Deutsches Zentrum
für Luft- und Raumfahrt

Institut für
Technische Optik

Initial Detection and Tracking of Objects in Low Earth Orbit

Master Thesis

German Aerospace Center Stuttgart,
Institute of Technical Physics,
Active optical Systems

University of Stuttgart
Institute of Applied Optics

Supervisors:

Prof. Dr. Alois Herkommer
University of Stuttgart

Paul Wagner, M.Sc.
German Aerospace Center Stuttgart

by
Thomas Hasenohr
(Matrikelnummer: 2972699)
Photonic Engineering

I. Abstract

For surveillance of the low Earth orbit (LEO) population the orbits of resident space objects (active satellites or space debris) has to be closely monitored. A possible solution for initial detection is the passive optical observation through wide-angle imaging systems with large fields of view (FOV). Based on measurements of these systems a short-time prediction of the object's trajectory can be determined which is sufficiently accurate to recapture it with a high resolution telescope during the same overpass of the object. In combination with laser ranging for distance determination, the information gathered by the telescope is precise enough to generate and maintain an independent catalog. This work presents such a system consisting of a wide-field imaging system (staring) and an astronomical telescope for recapture (chasing) and precise measurements.

Possible system set-ups are analyzed and evaluated based on the simulation tool PROOF (Program for Radar and Optical Forecasting) provided by the European Space Agency (ESA). These simulations result in a recommended pointing towards zenith for passive optical space surveillance, where the observation time starts 1.5 h after sunset and ends 1.5 h before sunrise. General calculations and corresponding PROOF simulations show the dependence of the aperture of the staring camera lens to the detectable object size. According to these simulations a camera system consisting of a FLI PL16308 camera and a 135 mm f/2.0 lens are a good combination with respect to the FOV (15.27° × 15.27°) and detectable size of 0.45 m. Per day 3422 different objects contained in the TLE- database are passing this FOV.

Furthermore the developed algorithm for initial object detection and tracking is presented. This algorithm is able to detect orbiting objects on a star background, assigns them to related detections from earlier images and predicts a future position for recapture the object with a high resolution telescope. The algorithm was tested at the DLR research observatory and the successful recapture is reported.

II. Zusammenfassung

Damit die Population des niedrigen Erdorbits überwacht werden kann, müssen die Objekte (aktive Satelliten oder Weltraumschrott) bekannt und katalogisiert sein. Weitwinkelsysteme mit großen Gesichtsfeldern stellen hierfür eine Methode für die Neudetektion dar. Basierend auf deren Messungen kann eine Kurzzeitprognose der Flugbahn des neu detektierten Objektes gegeben werden, die ein Wiedereinfangen mittels eines hochauflösenden Teleskops noch im selben Überflug erlaubt. Zusammen mit Laser Ranging zur Abstandsmessung sind die vom Teleskop ermittelten Informationen genau genug, um einen unabhängigen Katalog zu erzeugen und zu erhalten. Diese Arbeit präsentiert ein solches System zur Neudetektion bestehend aus einem Weitwinkelsystem und einem astronomischen Teleskop zum Wiedereinfangen und für genauere Messungen.

Mit dem Simulationstool PROOF der ESA wurden verschiedene Systeme analysiert und ausgewertet. Diese Simulationen führten zu einer empfohlenen Systemorientierung in Richtung Zenit, wobei die Observationszeit 1,5 h nach Sonnenuntergang beginnen und 1,5 h vor Sonnenaufgang enden sollte. Allgemeine Berechnungen und weitere PROOF Simulationen zeigen die Abhängigkeit des Aperturdurchmessers und der Brennweite von der detektierbaren Objektgröße. Laut diesen Simulationen ist eine gute Kombination für die Neudetektion von orbitalen Objekten eine FLI PL16803 Kamera ausgerüstet mit einem 135mm f/2 Objektiv, in Bezug auf das Gesichtsfeld von ($15.27° \times 15.27°$). Sie erlaubt es Objekte mit einer Größe von 0,45 m zu detektieren. An einem Tag würden im Schnitt 3422 verschiedene TLE- Objekte ein solches Gesichtsfeld passieren.

Des Weiteren ist der entwickelte Algorithmus zur Neudetektion von Objekten vorgestellt. Dieser ist in der Lage orbitale Objekte vor einem Sternhintergrund zu detektieren, sie zueinander zuzuordnen und eine Kurzzeitprognose zu ihrer Flugbahn zu erstellen, welche das Wiedereinfangen mittels Teleskop ermöglicht. Der Algorithmus wurde an dem Forschungsobservatorium des DLRs an der Uhlandshöhe in Stuttgart getestet und das erfolgreiche Wiedereinfangen von Objekten über die keine Vorabinformationen zur Verfügung standen ist präsentiert.

III. Danksagung

Ich bedanke mich ganz herzlich bei Herrn Riede am Institut für Technische Physik (DLR) für die Bereitstellung des Themas sowie bei Herrn Prof. Dr. Herkommer vom Institut für Technische Optik (ITO) für die Ermöglichung der Zusammenarbeit mit dem Zentrum für Luft- und Raumfahrt.

Ein besonderer Dank gilt Herrn Dr. Hampf für die Hilfe bei den Programmierarbeiten sowie den vielen wertvollen Anregungen bezüglich der Abschlussarbeit. Herrn Wagner danke ich für die Zusammenarbeit an diesem Projekt und für die Unterstützung bei Fragen im Bereich der Optik. Für die vielen hilfreichen Diskussionen bezüglich des Themas möchte ich Herrn Sproll, Herrn Dr. Humbert und Herrn Dr. Rodmann danken.

Ganz herzlich bedanke ich mich bei Herrn Dr. Humbert und Herrn Dr. Hampf für das Korrekturlesen der Abschlussarbeit. Des Weiteren bedanke ich mich allen Mitarbeitern der Arbeitsgruppe Aktive Optische Systeme für die kollegiale Zusammenarbeit während meiner Zeit am Institut.

Abschließend möchte ich Linda und meiner Familie danken, die mich während meines Studiums stets unterstützt haben.

IV. Table of Contents

1. Introduction

The growing number of space debris objects in low Earth orbit causes an increasing risk for active satellites and manned space missions. A collision in space does not only affect the operational work of a satellite. It can also cause a sudden growth of the debris population, which increases the threat for spacecraft even more. In 2007 the Chinese anti-satellite test and the accidental collision of the active Iridium 33 and the dysfunctional Cosmos 2251 in 2009 have increased the number of debris in LEO by about 60 % [1]. These two events are the reason for four of six close approaches of debris to the International Space Station in just 12 months (April 2011 to April 2012), when four collision avoidance maneuvers were necessary [2].

In order to avoid accidental collisions precise orbital information on resident space objects (RSO) is needed. Therefore the U.S. Space Surveillance Network (SSN) maintains a catalog containing over 40000 RSOs, in which more than 17200 are still in orbit [3]. The minimum size for cataloged debris is limited to about 10 cm for LEO objects and 70 cm for pieces in the geostationary Earth orbit (GEO) [4] due to the sensitivity of the detectors. About 85 % of the 17200 entries in this database are available as Two Line Element (TLE) catalog by the North American Aerospace Defense Command (NORAD) [5]. This makes it necessary to complement this catalog by initial detection of the missing RSOs for third parties.

Radars are the most common systems for LEO surveillance i.a. due to the independence of weather conditions. However, passive optical systems can be very efficient for LEO observations as well [6], despite the fact that these have been developed mostly for GEO surveillance. Passive optical systems are using the sun as illumination source and are able to detect small objects in LEOs as long as they are not in the Earth's shadow. In contrast to radar systems, space debris telescopes are cost effective and can operate unmanned like the French TAROT telescopes [7].

A system for initial detection of RSOs should be able to cover large regions of the sky for detecting as many passing objects as possible. The initial detection and subsequent precise measurements of the object's trajectory, which requires high image resolution, have to take place during the same overpass. Without the precise measurements the orbit information might be insufficiently known for adding the object to a catalog. Using wide FOV telescopes [8], [9] with FOVs of up to 10 ° are one method for precise position measurements of unknown RSOs. In order to reach large observed regions it is also possible to use multiple apertures with smaller FOVs [10]. A third possibility is used by the DLR in Stuttgart. Here an astronomical camera equipped with a telephoto lens is used for initial detection (staring). Afterwards a high resolution telescope is guided to a predicted position of the RSO (chasing) to perform accurate measurements. Such a system can be set up with commercial of the shelf (COTS) components and is able to reach FOVs up to 15.5 °× 15.5 °.

This work presents a "Stare and Chase" wide-angle system for initial LEO object detection and determination developed by the German Aerospace Center (DLR). In the second chapter an overview about the space population situation and the threats caused by space debris is given. Furthermore current methods for detecting and surveilling orbiting objects are shown as well as basics about astronomical coordinate systems and the determination of orbits based on optical sightings. The third chapter presents the Stare and Chase System at the Satellite-Laser-Ranging station at the Uhlandshöhe in Stuttgart. Its functionality and the used hardware are explained in detail. Performances of various set-ups of the staring camera based on the simulation tool PROOF by the European Space Agency (ESA) are analyzed in chapter four [11]. Additionally an optimal observation time and pointing direction of the camera system is determined. In the end of this chapter real measured data from the observation test bed is shown and compared to the results of the simulations. In the fifth chapter the requirements for a recapture of RSOs are showed based on a Monte Carlo simulation. Furthermore, different algorithms which were used for image processing are explained in detail. These are able to determine RSOs on a star background, assign objects of different images and extrapolate the trajectory of the RSO. The successful recapture of RSOs through the high resolution telescope without prior information is presented at the end of this chapter. The last chapter discusses the presented Stare and Chase system and the results of this work and gives an outlook for future improvements. Finally a set-up which is able to find and track orbiting objects is suggested.[1]

[1] Partial results of this master thesis were previously published in the paper "Initial Detection of Low Earth Orbit Objects through Passive Optical Wide Angle Imaging Systems" in September 2016, submitted for publication to the Deutsche Gesellschaft für Luft- und Raumfahrt at the Deutscher Luft- und Raumfahrtkongress September 2016.

2. General information about space surveillance

2.1. The space debris problem

Since the launch of the very first man made satellite Sputnik-1 into space on October 4, 1957, the Earth's orbit became more and more populated by spacecraft and junk. Figure 1 shows the increasing number of orbiting objects larger 10 cm during the recent 60 years. Smaller objects are more difficult to detect and there are no reliable numbers of the current population. There are about 700,000 objects larger 1 cm in orbit due to estimations [12]. Growing numbers of rocket launches in future and the very slow decay of objects into atmosphere will further increase the population in orbits of all altitudes [13].

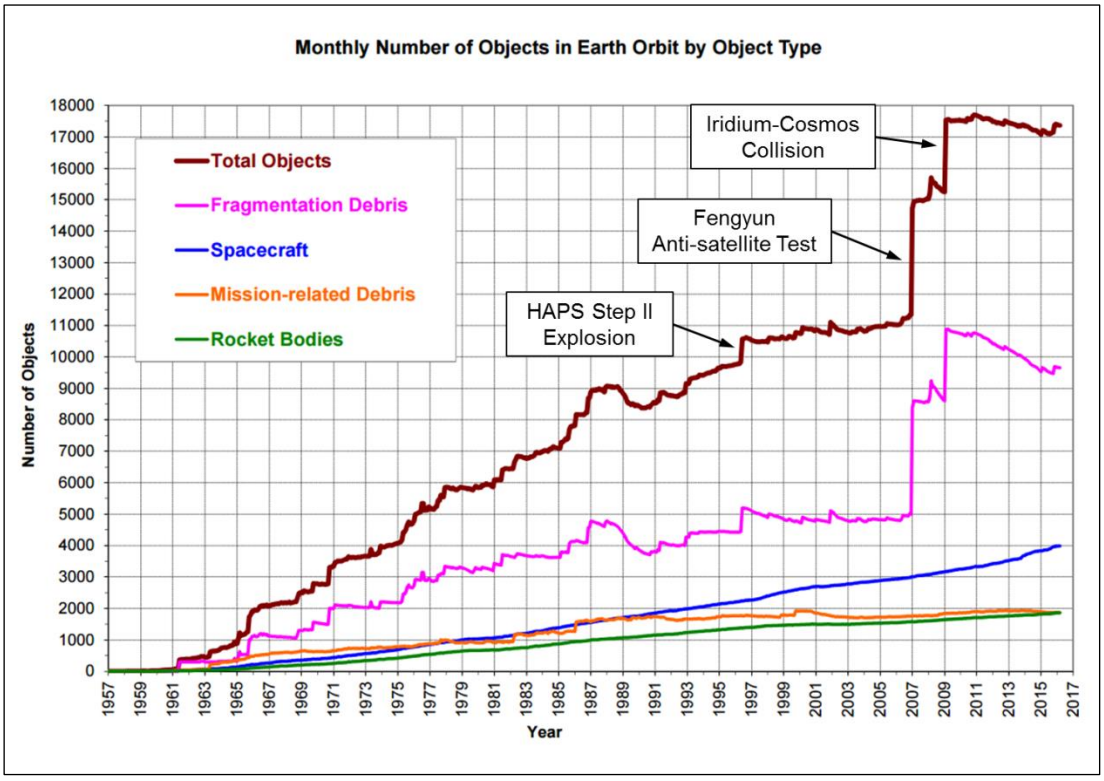

Figure 1: Increasing number of objects in Earth orbit over the last 60 years [14].

Currently about 94 % of RSOs are space debris. Officially space debris is defined as "(…) all man made objects including fragments and elements thereof, in Earth orbit or re-entering the atmosphere, that are non functional" [15] by the Inter- Agency Space Debris Coordination Committee. These fragments and elements are of different types and have a wide range of sources. It can be sorted in mission related objects like launch adapters and lens covers or leftovers from deployment of payloads like upper stages from rockets and inactive satellites. However, the major numbers of pieces belong to unintentional events [16]. These contain slag of rocket burns, degradation products from spacecraft like upper stages and satellites and most of all fragments from collisions. Other sources of space debris are explosions of rocket stages due to propellant, which remains often many years after launch.

One of the major threats of manned space traveling and for active spacecraft is the high number of space debris. Hence, the crew modules of the International Space Station (ISS) are shielded against impacts of objects up to 1 cm. Nevertheless the station has to execute flight maneuver to avoid collisions with larger space debris [2]. Providers of active satellites also have to fly these maneuvers to guarantee an operating system.

In Earth orbit the density of RSOs is not equally distributed. At some regions it is much higher and other regions are almost free of debris. For LEO the density of space debris is highest at an altitude of about 800 km but also at an altitude of about 1450 km the number of RSOs is increased (figure 2). The reasons are the good conditions for remote sensing and space weather [17]. In these very dense regions the collision risk of space debris is increased strongly. Many missions have a near polar orbit, which increases the risk even more at Polar Regions. Another accumulation is the geostationary orbit (GEO) at an altitude of 35,786 km above equator. Here the revolution around Earth of one satellite takes exactly one sidereal year. This leads to exactly the same location in the sky at all times, which is used for example for TV- satellites.

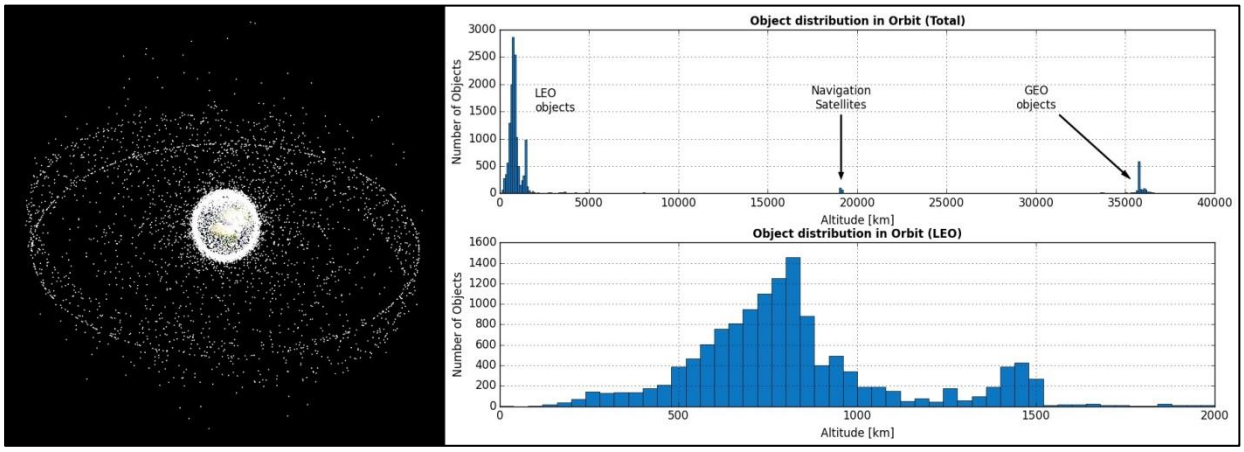

Figure 2: Earth with orbiting space debris (left) [DLR / L. Humbert]. Altitude distribution of space debris orbiting Earth (right) (Data from 2016-04-01 [5]).

Most space debris does not remain forever in an orbiting position. Lifetimes of RSOs without any flight maneuver depends strongly on the altitude of the orbit. High altitudes lead to long lifetimes, while low altitudes are resulting in an early decay of the RSO (see figure 3). GEO satellites and space debris at such heights will remain in space forever, because the distance from Earth is too far and no drag occurs. The increasing density of the atmosphere causes a growing drag to the RSO the lower the orbit gets, which slows the object down and leads to an even lower altitude. Additionally, Earth's- , solar- and lunar gravity as well as solar pressure forces objects off their trajectory, too, even on high altitudes. Friction heat burns the re-entering object when the RSO is too slow. In order to maintain a stable orbit on an average altitude of 386 km and to avoid a re-entering the International Space Station (ISS) has to fly several maneuvers every year.

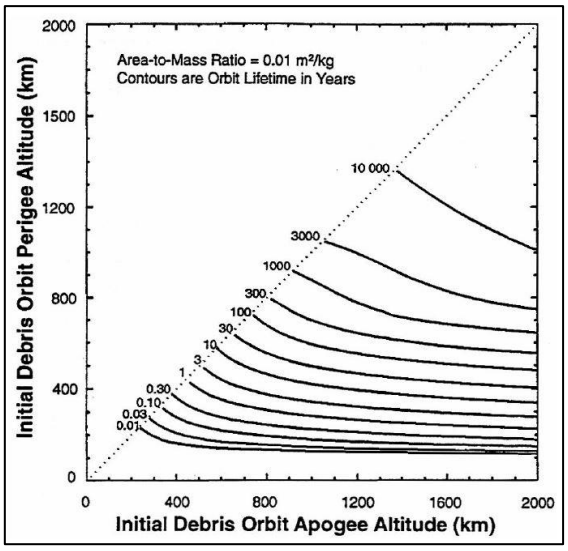

Figure 3: Lifetime of space debris in low Earth orbits [18].

Continuous detections of RSOs are necessary due to the mentioned influences of the orbits. Otherwise the information about the objects location is inaccurate and threat analysis for active satellites or manned spacecraft is not reliable any more.

2.2. Astronomical coordinate systems

There are many different astronomical coordinate systems. Each of them has its own field of application. For giving an overview the most important systems are explained in the following:

2.2.1. Horizontal Coordinate System

Origin of the horizontal coordinate system is the location of the observer, where horizon is used as the fundamental plane [19] (see figure 4).

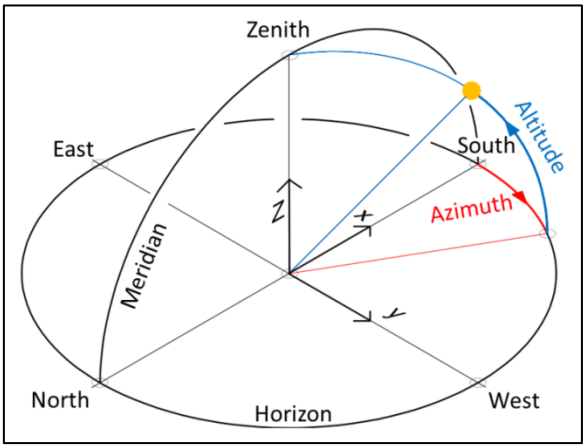

Figure 4: Schematic figure of the Horizontal Coordinate System for the northern Hemisphere [20].

Two angles which are called azimuth and altitude describe the position of an object in this system. Therefore it is also known as altitude-azimuth coordinate system. Beginning from North the azimuth is measured eastward in degrees, arc minutes and arc seconds. From horizon to the

zenith the altitude is measured in the same units. This system is relative to the location of the observer which causes a movement of the object's position in space due to Earth's rotation.

2.2.2. Equatorial Coordinate System

The equatorial coordinate system's fundamental plane has the same attitude as the Earth's equator but is expanded to infinity, called the celestial equator [21]. Its origin may be Earth's center (geocentric) or the location of the observer at any point on the surface of the Earth (topocentric). The X axis of the system is pointing from its origin to the vernal equinox direction, which is this direction where the Sun's center is located at the first day of spring. Pointing in direction North Pole beginning from Earth's center is the Z axis. Keep in mind that this system does not rotate with Earth's rotation. Any object in the "celestial sphere" can be measured by two angles, the right ascension and the declination. The right ascension encloses the vernal equinox direction and the direction of the target on the fundamental plane. It is measured eastward beginning from vernal equinox direction. Northward from the celestial equator to the Celestial North Pole the declination is measured. Due to the enormous distance the stars will remain almost at the same position, even after a half orbit of Earth around the Sun and the coordinates are known very well (smaller than one arc second). However a moving object in Earth orbit has changing coordinates. Therefore the coordinate system can be used for determination of Earth satellite's spatial location.

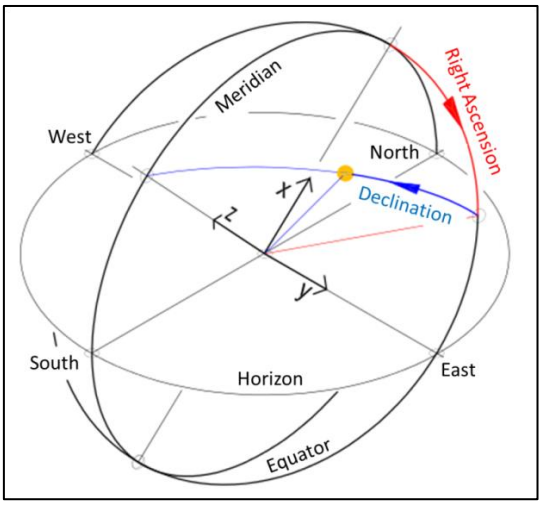

Figure 5: Schematic figure of the Equatorial System [20].

2.3. Current techniques for space debris surveillance

For surveillance of space debris and the locations of operating satellites two basic observation methods are used with different advantages and disadvantages [16]. Both methods are based on detecting electromagnetic waves. These waves are partially absorbed through the atmosphere surrounding Earth except two applicable windows (see figure 6). One of the windows is the optical window which contains wavelengths between 0.2 µm to 2 µm. The other one is at

wavelengths of 1 cm to 10 m and can be used for radar measurements. Mostly the surveillance of LEO orbits is accomplished by radars, however higher altitudes are observed by optical systems. These two techniques, their advantages and disadvantages are discussed in the following subsections.

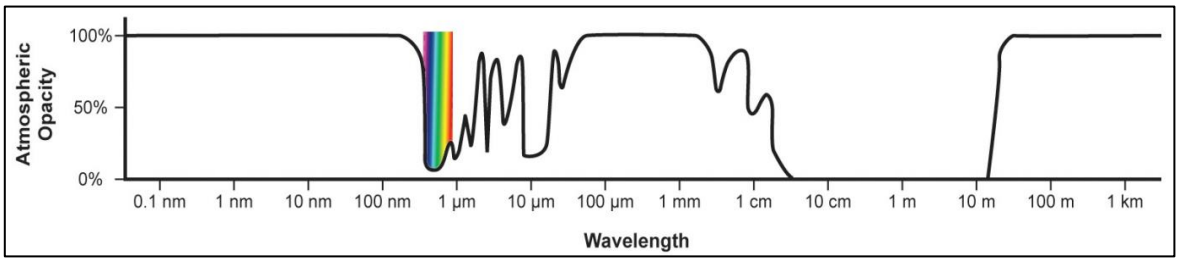

Figure 6: Atmospheric Opacity for different wavelength [22].

2.3.1. Optical techniques

Optical space surveillance techniques are mainly based on passive optical methods. For passive optical measurements the target is illuminated by an external source. In the case of space surveillance the source is the sun. The light is reflected by an RSO and the reflection can be detected by an optical system on ground or space. How bright an RSO appears to be depends on the distance, on the albedo of the object and the phase angle. In section 3.2, the collected energy of the optical system will be explained in more detail.

There are two kinds of telescopes: Refractor telescopes which are based on light refraction of lens systems and reflector telescopes, where the light is reflected on several mirrors. An advantage of reflective telescopes is the availability of large apertures. Refractive telescopes are limited technically to apertures on the order of 1 m, while the reflective telescopes can reach up to 10 m in diameter. Other advantages are the lower production costs, the better performance in image resolution, color correction and a lower mass of the telescope for large apertures. Reflective telescopes can be separated into basic design types which are shown in figure 7.

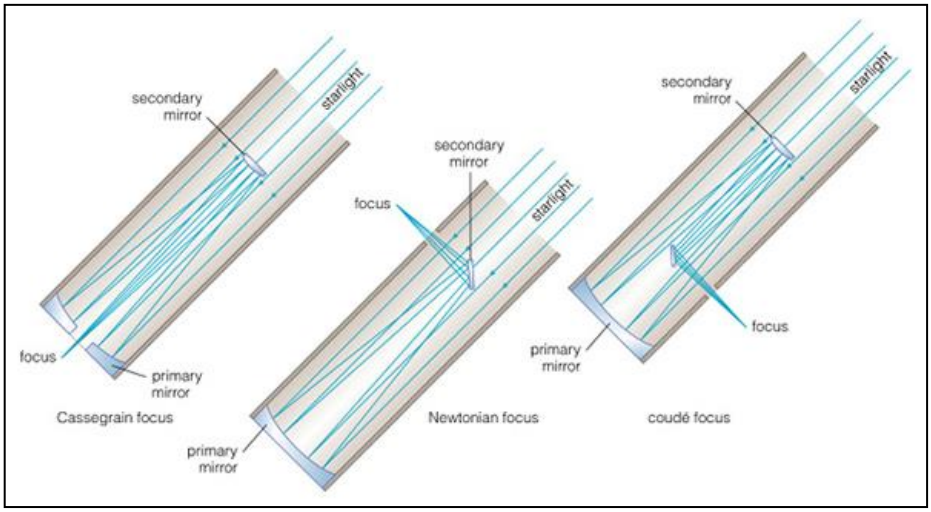

Figure 7: Profile of a Cassegrain, a Newtonian and a Coudé telescope [23].

Planar secondary mirrors are built in Newton telescopes (figure 7 in the center) and can reach f-numbers from 3 to 5 [16]. Cassegrain telescopes (figure 7 left hand side) are set up with convex shaped secondary mirrors and f-numbers ranging from 8 to 20. This kind is also possible with correcting lenses arranged in the hole of the primary mirror, then called Ritchey- Chrétien telescope. The third type is a Coudé telescope (figure 7 right hand side). It has an additional secondary mirror which is planar and reflects the light to a separate Coudé room where stationary equipment can be located. Typical f-numbers are between 30 and 50.

An optical sensor converts the focused light into an electrical signal for subsequent computer processing. Mainly Charged-Coupled Devices (CCD) or metal oxide semiconductors (MOS) are used as imaging sensors. A fast readout is the advantage of the MOS sensors but the CCDs are convincing with their low signal-to-noise ratio. Resolutions can be achieved as high as 0.5 arcseconds due to the performance of the optical design and the high pixel density of the imaging sensors. This number is a theoretical value and changes to about 1.0 arcsecond [16] caused by the seeing (atmospheric turbulences).

The United States Space Surveillance Network (SSN) and the Russian Space Surveillance System (SSS) are already providing operating optical observation sites for maintaining their catalogs for high altitudes [16]. In Europe and Japan some sites are already operational but none of them is maintaining a catalog (as on 2013). Figure 8 shows the operating Space Debris Telescope at the Teide Observatory on Tenerife provided by ESA. Its main aims are observations of the geostationary ring. This telescope has a 1 m aperture, a FOV of 0.7 ° and is of a Cassegrain type. A Coudé focus for optical communication applications and a Ritchey-Chrétien focus for space debris observation can be used.

Figure 8: The ESA Space Debris Telescope at the Teide Observatory, Tenerife [24].

2.3.2. Radar supported techniques

Currently the most common method for space surveillance of LEO altitudes is observation by radar [16]. Towards shorter wavelengths the applicable atmospheric transmission window is limited to resonant effects of water vapor. Reflections and attenuations in the ionosphere limits the window to longer wavelengths.

Radar facilities are emitting radio waves and detecting the reflection by the target. Measurements of the signal's time of flight determine the distance between a ground station and a target. Additional information about the target is gathered by the measurement are: The location (given by azimuth and elevation), the range rate (given by the two-way-Doppler-shift) and the radar cross section (RCS), material, shape and orientation (given by the echo of the signal and the polarization change of the radio wave). The received power depends on the emitted power, the area of the emitter and receiver, the used wavelength, the range and the RCS of the object. Emitter and receiver radar can have different sensor sizes, where the receiver has a larger antenna or antenna array. This is the case for bi-static or multi static systems. Mono static systems are using the same radar antenna for emitting and receiving.

There are two basic kinds of radar stations, reflector radars and phased array radars. Reflector arrays have a parabolic dish and are steerable in the horizontal plane. Due to the dish they are limited in the FOV similar to optical systems. Therefore these radars are mostly used for tracking specific objects. Such a radar system is provided by the Fraunhofer Institute for High Frequency Physics and Radar Techniques (FHR) near Bonn and is called Tracking and Imaging Radar (TIRA). The parabolic dish antenna has a diameter of 34 m and is operated at a wavelength of 22.5 cm with a peak power of 1 MW for tracking duties. It is able to track objects as small as 2 cm at altitudes of 1000 km, if it is used as transmitter radar. The Radio Telescope Effelsberg (diameter of 100 m) operated by the Max Planck Institute for Radio Astronomy 21 km away is used as a receiving radar for this operational mode. Phased array radars are used to observe wider regions. Such radars are large arrays of more than 10,000 antennas and are able to cover regions of up to 120 ° FOV. This large FOV allows tracking many objects at the same time. Unlike the reflector radars they are not steerable.

Currently the most important radar for space surveillance is a phased array radar at Eglin, Florida [16], shown in figure 9. Its transmitter radar has a diameter of 29 m whereby the receiver radars 58 m in diameter. The FOV of 105 ° combined with its location and orientation allows the detection of about 95 % of all catalog objects in LEO with a detection rate of 50,000 objects per day. The peak power reaches 32 MW at a frequency of 442 MHz.

Figure 9: Phased array space surveillance radar at Eglin, Florida [25].

The French GRAVES system (Grand Réseau Adapté à la Veille Spatiale) provided by the French Department of Defense is the only European installation outside US SSN and the Russian SSS, which performs space surveillance. It is able to detect object sizes lager than 1 m at 1000 km altitude.

2.3.3. Advantages/disadvantages for radar- and optical systems

At the moment radar surveillance is mostly used for LEO and close Medium Earth Orbits (MEO) where higher altitudes are observed by optical facilities [16]. This is caused by the limited range of radars due to the active illumination of the target with radio wavelengths. Optical observation allows using the sun as illumination source which leads to a signal distance which is half the way of a radar signal for the same target.

The major advantage of radar is the independence of meteorological and daytime conditions. Wavelengths, emitted by radar stations are able to penetrate clouds, where an optical system cannot be used. Also the ambient light has no effects, due to radars sensitivity at exactly the emitted wavelength. Optical telescopes must be used at night or in twilight, when the ambient light is negligible. This also includes artificial light which means that a telescope site should not be close to light sources like cities due to light pollution. However, the extremely high costs of radars compared to optical systems make an optical LEO surveillance interesting. This allows building a global covering network of telescopes. Such a network could eliminate all the disadvantages of individual optical systems.

Another very important advantage of optical space surveillance for LEOs is that the angular pointing accuracy and resolution of optical sensors is higher than the radar resolution. Therefore most accurate orbit determination can be achieved by optical telescopes. Table 1 gives an overview over the presented advantages and disadvantages of optical and radar surveillance methods.

Table 1: Advantages and Disadvantages of optical and radar surveillance.

	Radar	Optical
Advantages	Independence of weather conditions	Low costs
	Independence of daytime	Pointing accuracy
	Large FOV	No limitations in range
	More information about object	
Disadvantages	Limitations in range	Weather conditions
	High costs	Ambient light

2.4. Methods for orbit determination from optical observation

The orbit determination of a passing object is due to its complexity not part of this thesis but one method will be explained for giving an overview of difficulties and the needed parameters. In order to describe an object's orbit six elements are necessary. These elements are the semi-major axis, the eccentricity, the inclination, the longitude of the ascending node, the argument of periapsis and the time of periapsis [21]. Figure 10A shows the elements simplified in a model for an orbiting object. One method for determination of an orbit uses six components of the location for specific dates and the correlating velocity vectors. This method will be explained in the following.

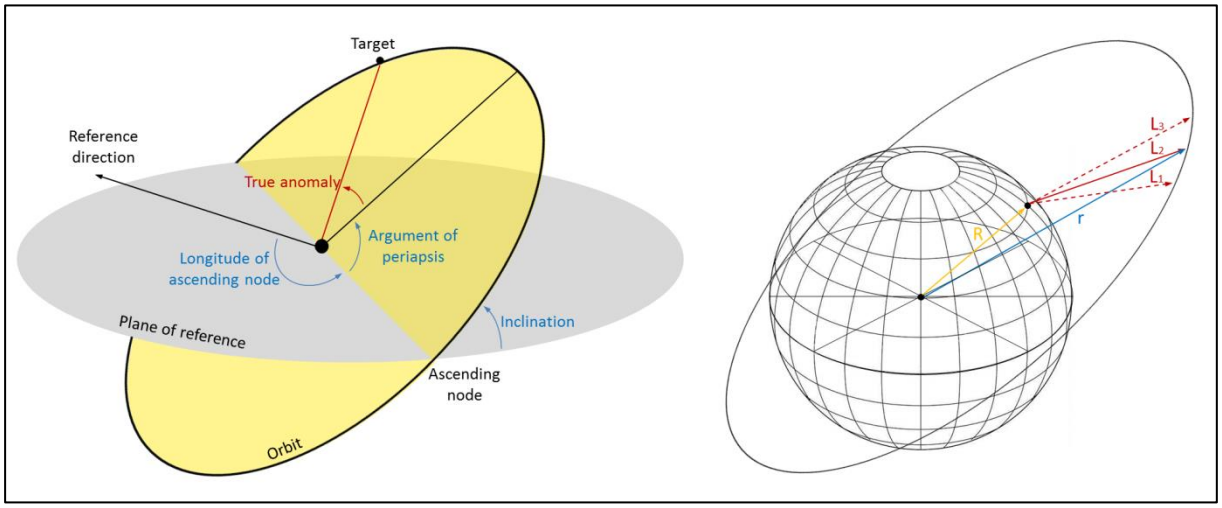

Figure 10: Figure A (left): The six needed parameters for orbit determination shown on a reference plane and an orbit of a satellite. Figure B (right): The measured LOS vectors of an observation site (red) in context to the location vector(blue) of the satellite.

The shown method uses the optical sight of the object [21]. One optical observation gives just two independent quantities which are the azimuth and altitude or the right ascension α_i and declination δ_i. Therefore three successive observations at three different times are necessary to get the needed elements. The measured coordinates have to be converted into two vectors. First, a location vector of the object *r* with its base at the center of Earth and second a velocity vector *v* of the Object in direction of the trajectory. With these two vectors for each observation, the orbit can be successfully determined.

First the vectors must be calculated. The only vectors which can be determined directly are the line of sight (LOS) vectors L_i (see figure 10B) with their base at the observation site. These are given by the matrix

$$\boldsymbol{L_i} = \begin{bmatrix} \boldsymbol{L_I} \\ \boldsymbol{L_J} \\ \boldsymbol{L_K} \end{bmatrix} = \begin{bmatrix} \cos\delta_i & \cos\alpha_i \\ \cos\delta_i & \sin\alpha_i \\ \sin\delta_i & 1 \end{bmatrix}_i , i = 1, 2, 3. \tag{2.4-1}$$

L_i are unit vectors and the range to the target is unknown. Therefore a slant range ρ has to be used for determination of the distance from the location site to the object. For getting the location vector r based on the center of the Earth

$$\boldsymbol{r} = \rho\boldsymbol{L} + \boldsymbol{R} \tag{2.4-2}$$

must be used as geometric formula, where R is the vector from Earth's center to the observation site. The used vectors are shown in figure 10B. After a differentiating equation (2.4-2) twice the formula becomes to

$$\ddot{\boldsymbol{r}} = 2\dot{\rho}\dot{\boldsymbol{L}} + \ddot{\rho}\boldsymbol{L} + \rho\ddot{\boldsymbol{L}} + \ddot{\boldsymbol{R}} . \tag{2.4-3}$$

In the equation of motion for a two body problem:

$$\ddot{\boldsymbol{r}} = -\mu\frac{\boldsymbol{r}}{\mathrm{r}^3} \tag{2.4-4}$$

μ represents the gravitational parameter, r the location vector of the target and ɼ the range from Earth's center to the object. Combining this equation (2.4-4), equation (2.4-2) and equation (2.4-3) gives the following expression:

$$\boldsymbol{L}\ddot{\rho} + 2\dot{\boldsymbol{L}}\dot{\rho} + \left(\ddot{\boldsymbol{L}} + \frac{\mu}{\mathrm{r}^3}\boldsymbol{L}\right)\rho = -\left(\ddot{\boldsymbol{R}} + \mu\frac{\boldsymbol{R}}{\mathrm{r}^3}\right). \tag{2.4-5}$$

Herewith, the needed orbit parameter can be determined through its determinant and the Cramer's rule. However, just the quantities of L, R and $\ddot{R}$ are known yet for a specific time. $\dot{L}, \ddot{L}, \rho, \dot{\rho}, \ddot{\rho}$ and r have to be calculated before the determination of the velocity- and location vectors of each epoch. L is known due to a Lagrange interpolation formula (2.4-6) and the three measurements. $\dot{L}$and $\ddot{L}$ can be determined by differentiation ((2.4-7) or (2.4-8)):

$$\boldsymbol{L}(\boldsymbol{t}) = \frac{(t-t_2)(t-t_3)}{(t_1-t_2)(t_1-t_3)}\boldsymbol{L_1} + \frac{(t-t_1)(t-t_3)}{(t_2-t_1)(t_2-t_3)}\boldsymbol{L_2} + \frac{(t-t_1)(t-t_2)}{(t_3-t_1)(t_3-t_2)}\boldsymbol{L_3}\,, \tag{2.4-6}$$

$$\dot{\boldsymbol{L}}(\boldsymbol{t}) = \frac{2t-t_2-t_3}{(t_1-t_2)(t_1-t_3)}\boldsymbol{L_1} + \frac{2t-t_1-t_3}{(t_2-t_1)(t_2-t_3)}\boldsymbol{L_2} + \frac{2t-t_1-t_2}{(t_3-t_1)(t_3-t_2)}\boldsymbol{L_3}\,, \tag{2.4-7}$$

$$\ddot{\boldsymbol{L}}(\boldsymbol{t}) = \frac{2}{(t_1-t_2)(t_1-t_3)}\boldsymbol{L_1} + \frac{2}{(t_2-t_1)(t_2-t_3)}\boldsymbol{L_2} + \frac{2}{(t_3-t_1)(t_3-t_2)}\boldsymbol{L_3}\,. \tag{2.4-8}$$

Numerical values for example for the second measurement are available after setting t = t_2. More accurate numbers are available, if more than three observations are used.

Now, Cramer's rule can be applied to equation (2.4-5) which solves it for ρ. The solution is ρ as a function of r and can be solved for r at the t_2 by iteration. Finally, ρ can be determined and with equation (2.4-2) r as well.

In the end the velocity vector must be determined for full orbit information. The calculations are equal to the determination of the location vector, hence, using the Cramer's rule for solving the equation for $\dot{\rho}$. The solution is a function of r again. In order to get v it is necessary to differentiate equation (2.4-2) and insert the known quantities into the expression (2.4-9):

$$\boldsymbol{v} = \dot{\boldsymbol{r}} = \dot{\rho}\boldsymbol{L} + \rho\dot{\boldsymbol{L}} + \dot{\boldsymbol{R}}. \tag{2.4-9}$$

However, this method fails, if the observation site is in the plane of the object's orbit and other methods have to be used.

The shown orbit determination is just one method, but many more are known. It is for example possible to combine two optical measurements with the Coordinated Universal Time (UTC) or using all the parameters given by one measurement by radar observations. All these calculations and other approaches for determination of an objects orbit are shown in reference [21] in more detail.

2.5. Two Line Elements (TLE)

In order to catalogue Earth orbiting objects the North American Aerospace Defense Command (NORAD) and the National Aeronautics and Space Administration (NASA) developed the Two-Line Element (TLE) [16]. Such an element contains all the information, which is needed for determination of the state of an object at any time. These states are for example the position or the velocity of an RSO. The TLE database is not recommended for precise analyses by the TLE providers because of the insufficient accuracy of the RSO coordinates and missing errors [26].

All TLEs are saved in an ASCII text file and each element consists of two lines of 80 characters [27]. Sometimes each element has an additional entry ahead with satellite- or rocket name and number. Each line starts with the satellite number to ensure the right assignment [4]. The first line consists of classification, information about launch and the atmospheric drag. Information about the orbit is found in the second line. Following an example of the ISS as TLE object is shown [5]:

```
ISS (ZARYA)
1 25544U 98067A   16133.73910976  .00008193  00000-0  12878-3 0  9996
2 25544  51.6441 234.8623 0002754 119.2388 339.6420 15.54576296999465
```

The elements listed are based on the observation data from the SSN by the United States. Because of the sensitivity of the optical- and radar systems the minimum size of objects for LEO is about 10 cm and 70 cm for GEO objects. Objects smaller than these values are not included and therefore no information about their orbits are known.

More than 15,000 entries are contained by the current NORAD catalog where active satellites are included. However, the total number of the SSN-known objects is larger 40,000 objects where over 17,200 are still in orbit (see figure 1) [3]. The catalog is based mainly of radar systems for LEO and optical systems for Medium Earth Orbits (MEO) and GEO altitudes. Russia maintains its own catalog provided by the SSS with about 30% fewer objects than NORAD. This difference results due to a lack of sensor systems at lower latitudes and a different detection threshold.

For further information like the RCS, origin and decay or apogee and perigee distance of the RSO, the Center for Space Standards & Innovation provides a satellite catalog (SATCAT) [5] containing the SSN- known objects. However, the geometric shape and size of an object is mostly unknown. Approaches for converting the RCS to an optical size are given and explained in the reference [28] but have to be treated with caution due to many different influences like the objects material.

3. DLR testbed

Since 2013 the DLR is developing a research observatory at the Uhlandshöhe in Stuttgart called Uhlandshöhe Forschungs Observatory (UFO), which is shown in figure 11. Its major purposes are passive and active optical observations of LEO objects.

Figure 11: DLR research observatory at the Uhlandshöhe, Stuttgart.

Originally the UFO was set up for developing a fiber based Satellite Laser Ranging (SLR) system. SLR can be used for example for precise orbit determination (e.g. collision avoidance) or geodesy (e.g. tectonic plate drifts). The time of flight of a laser pulse is measured and gives accurate distance information about the target [29]. Directing the light from the laser source to the transmitter telescope with an optical fiber instead of using a coudé path is unique for a SLR station. A Nd:YAG laser serves as laser source emitting light with a wavelength of 1064 nm. Pulses with a duration of 3 ns at a power of 300 µJ are used for the measurements of the targets distance. The first successful satellite ranging to a satellite was accomplished in December 2015 [30].

Currently two different passive optical approaches are used for orbit surveillance and for improving orbit forecasts will be developed. First, the “Stare and Chase” which is the subject of this thesis is explained in the following sections in more detail. Second the measurement of light curves of RSOs, which can be determined while tracking an object with a telescope. The detected light intensity depends on the reflection of the RSO illuminated by the sun. Hence, the reflection depends on the angle of incidence of the light, which could change due to a spin of the RSO. Therefore, the spin can be determined by measuring the light curve for a specific period. It provides information which can be used for improving the forecast of an objects orbit and determining its state.

3.1. Stare and Chase

The “Stare and Chase” system is a passive optical approach for initial detection and tracking of objects in LEO. Main components are an astronomical camera with a telephoto lens which serves as wide angle imaging sensor. A 17 inch (432 mm) telescope is mounted on an astronomical mount for precise angular coordinate measurements and a computer system for image processing and telescope control.

An astronomical camera equipped with an exchangeable, commercially off-the-shelf lens “stares” into the night sky in a specific direction and takes images continuously with typical exposure times ranging from 0.05 s to 1 s. The short focal length of the staring system leads to a wide FOV and therefore a large observed region of the sky compared to telescopes. During the overpass of an object within the FOV, an image processing algorithm extracts the object’s position and determines if it is already contained in the TLE catalog. Furthermore a short-time prediction of the estimated object’s trajectory is calculated giving the equatorial coordinates after a specific time. For recapture (“chase”) the object, the predicted coordinates are forwarded to the high resolution telescope. The camera of the high resolution telescope takes an image exactly at the time corresponding to the prediction. This enables a high resolution measurement of the angular coordinates of the initially unknown object. Subsequent laser ranging e.g. with a system presented in [30] could allow generating even more precise orbit information. Figure 12 shows the simplified system architecture and the sequence diagram for operation.

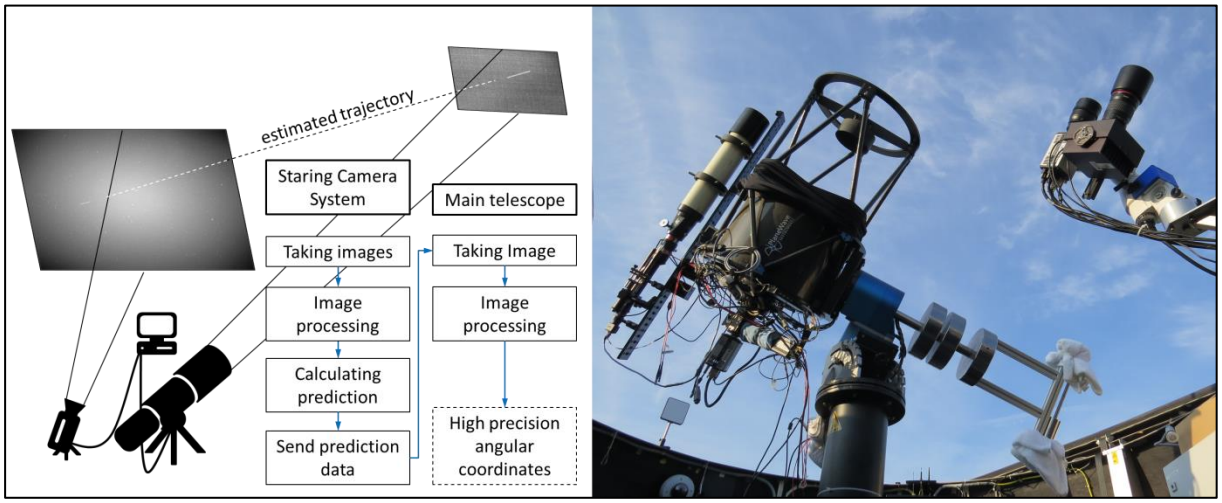

Figure 12: Block chart of the Stare & Chase system and the simplified system design (left). The Stare & Chase system at the Uhlandshöhe, Stuttgart.

This method for space surveillance can be used to set up a database or maintaining an existing one. For catalog maintenance the algorithm can be adjusted to track only unknown objects by the telescope or objects for which the available information is invalid.

Astronomical telescopes besides special models are not useful for the initial detection of RSOs due to the very limited FOVs of less than 0.5 °. Hence, staring cameras are used, which can obtain FOVs typically from 5° to 25° FOV.

3.2. General considerations

In theory the best solution for the parameters of the staring camera lens can be calculated. Most important is the amount of energy of the light which is collected per camera pixel. The longer the exposure the brighter appears the object in the image and the higher the contrast. The focal length and aperture diameter of the lens defines the amount of the received light, but it depends also on object parameters for example altitude, size and albedo. For simplicity and due to the object's small size related to its distance a point like source of light is considered.

It is necessary to know the exposure time of an RSO on one pixel of the camera. This information is based on the angular resolution R_P of one camera pixel which has to be determined first. Equation (3.2-1) shows its dependence on the focal length f' of the used lens and the pixel size of the sensor chip s_P:

$$R_P = \tan^{-1}\left(\frac{S_P}{f'}\right). \tag{3.2-1}$$

The first cosmic velocity describes the speed of an object orbiting Earth. If it would be faster it would leave this orbit, otherwise it would re-enter Earth's atmosphere. For simplicity it is considered that the RSOs are on circular orbits, which is a common approximation for LEO objects and is given by:

$$v_{sat} = \sqrt{\frac{G * M_{Earth}}{r_{Earth} + alt}}. \tag{3.2-2}$$

A satellite's velocity (equation (3.2-2), [31]) depends on the gravitational constant G, the Earth's mass M_{Earth} and the altitude above the orbit's origin at Earth's center (r_{Earth} + alt). The angle φ enclosed by the RSOs positions after a distance of time t_P is given by the velocity, the altitude and the time itself:

$$\varphi = \tan^{-1}\left(\frac{v_{sat} * t_P}{alt}\right). \tag{3.2-3}$$

In equation (3.2-3) the circular shape of the covered distance of an RSO in one second is approximated onto a straight line due to the high altitudes of over 800km (small-angle approximation). Equate the pixel resolution R_P by the angular velocity φ gives the time of an RSO on one pixel of the camera t_P:

$$t_P = \frac{s_P}{f'} * \frac{alt}{v_{sat}}. \tag{3.2-4}$$

The irradiance from the illuminated object E_{Obj} and the aperture of the camera lens A_A give the received power P_{Obj}. Equation (3.2-5) shows the correlation of theses quantities. For determining the optimal lens the irradiance is fixed to a specific value. In order to get a value of this quantity, it would depend on the distance from the lens to the target, the atmospheric conditions, the albedo of the object, the phase angle of the reflection and the distance from the object to the sun:

$$P_{Obj} = E_{Obj} * A_A \,. \tag{3.2-5}$$

Finally, the energy collected by one pixel E_P can be calculated, if the optical quality of the imaging system is sufficiently good to focus the RSO on just one pixel, which is assumed for this calculation. It is the received power of the RSO during the exposure time of a pixel:

$$E_P = P_{Obj} * t_P \,. \tag{3.2-6}$$

Extending the time of an RSO on one pixel or the received power increases the collected energy. Merging equations (3.2-4), (3.2-5) and (3.2-6) give an overview of the influences of the several parameters:

$$E_P = E_{Obj} * A_A * \frac{s_P}{f'} * \frac{alt}{v_{sat}} = E_{Obj} * \frac{1}{4} * \pi * d^2 * \frac{s_P * alt}{f' * v_{sat}}. \tag{3.2-7}$$

According to this equation the received energy increases with the power of two of the lens diameter d but decreases with an extension of the focal length. This is caused by a faster movement of the image of the RSO over the camera chip and therefore a decreased exposure time on one pixel if the focal length is longer. For compensating this problem the sensor pixels should be as large as possible. However, the resolution of the camera and therefore the prediction accuracy of the RSO's trajectory decrease with large pixels (see section 5.1).

An optimal camera lens for this case would have a very large aperture and a very short focal length which leads to small f-numbers. However f-numbers below one are technically difficult to manufacture, due to occurring optical aberrations which have to be compensated. According to equation (3.2-7) increasing the aperture diameter has much higher effects than decreasing the focal length of the lens.

Equation (3.2-4) can also be used to determine the optimal exposure time for space surveillance. It is just necessary to expose the image sensor as long as the object moves over exactly one pixel.

The received light could be too little for detection due to the background noise if a shorter time is used. For a longer exposure times which causes longer tracks of an RSO on the image, the signal-to-noise ratio decreases because of the increasing dark noise per time unit. However, due to the large region of LEO with altitudes between 800 km and 2000 km and therefore different angular velocities a compromise has to be found. Figure 13 shows typical exposure times for different lenses which are equipped to a camera with a pixel size of 9 µm with respect to the distance of the RSO to the observation site.

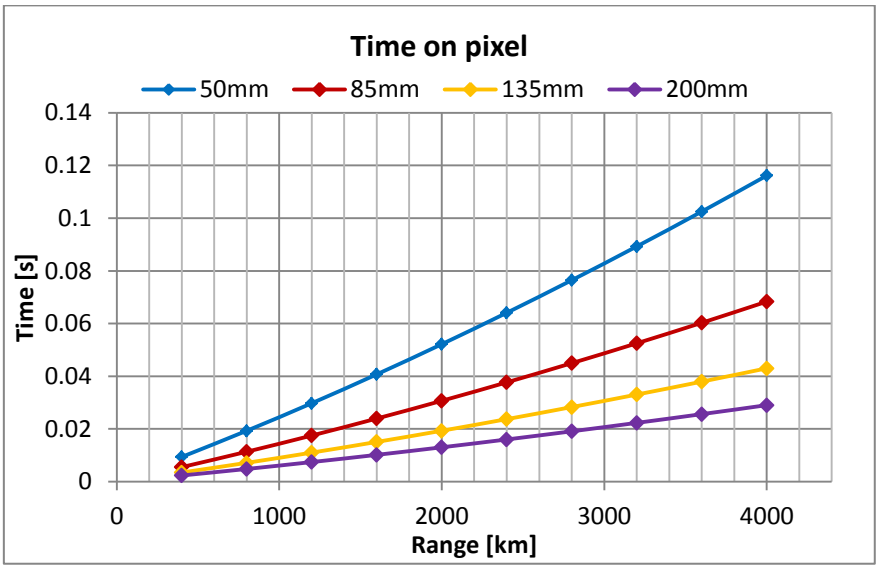

Figure 13: Time of an RSO on one pixel with respect to its distance from the camera system.

3.3. Hardware

In order to operate a Stare and Chase system many different hardware components are needed and have to communicate with each other. The used hardware of the DLR observation site besides the computers will be explained in this section:

3.3.1. The Telescope

The main telescope (see figure 14) is a corrected Dall-Kirkham telescope with an aperture of 17 inch (432 mm) [32]. A Dall-Kirkham design is an advanced version of a Cassegrain telescope design (see subsection 2.3.1). Differences are the elliptical primary mirror instead of a parabolic shaped and a spherical secondary mirror instead of a hyperbolic one. The resulting coma and field curvature is corrected through a two element corrector lens with broadband AR coatings. Its 2939 mm focal length and the used Andor Zyla CMOS camera (more details in subsection 3.3.2) are yielding a FOV of $0.32° \times 0.27°$.

Figure 14: The 17" main telescope, used to recapture the detcted RSOs.

An equatorial mount is carrying the telescope and further equipment. It is used as receiver telescope for SLR and as main telescope for the passive optical measurements. On top of the telescope a smaller “emitter” telescope is attached which is used for emitting the laser beam for SLR. However, it is not used for passive optical measurements and therefore not explained in more detail.

3.3.2. The Staring Cameras

Two different staring cameras were investigated (figure 15). The first astronomic camera is a ProLine 16803 from Finger Lakes Instrumentation (FLI). Its sensor is a CCD, which is optimized for low noise. The second camera is a Zyla from Andor. It is a CMOS type senor chip with the advantage of a fast readout. For the main telescope the same camera type is used. Specific data of the two cameras are shown in table 2. Both cameras are installed at an azimuth-elevation mount, which is aligned to a fixed direction. As data link to the image processing computer USB2.0 (FLI) and Camera Link (Andor) is used.

Table 2: Parameters of the used astronomical cameras [33], [34]

	FLI PL16803	Andor Zyla
Sensor	CCD (Front Illuminated)	CMOS (Front Illuminated)
Pixels	4096x4096	2560x2160
Pixel Size	9µm	6.5µm
Sensor Size	36.8mm x 36.8mm	16.6mm x 14.0mm
Readout Noise	14e-/px	2.9e-/px
Dark Current	0.005e-/px/s	0.14e-/px/s
Maximum Quantum Efficiency	60%	60%
Interface	USB2.0	Camera Link

A large pixel size of the FLI camera allows detecting faint objects. This pixel size and the high number of pixels together with the used lenses are leading to a wide FOV. A disadvantage of this

camera is the mechanical shutter which takes almost 40 ms for opening and closing [35]. This delay can cause inaccuracies in predicting the location for recapturing. The pixel size of the Andor Zyla camera is smaller which results in less collected light per pixel. It occurs due to the shorter exposure of the pixel and the focus spot size which is larger than one pixel (see subsection 3.3.3). For short exposure times the low readout noise compensates this disadvantage. An overall smaller sensor leads to a smaller FOV compared to the FLI camera. However, a fast readout speed allows high frame rates, which can be useful for multiple detections of fast objects. Furthermore it has an electronic shutter which does not cause a delay of the exposures.

Figure 15: The two staring cameras from Andor (left) and Finger Lake Instruments (right).

Both cameras can be equipped with different camera lenses which are presented in the following subsection in more detail.

3.3.3. The staring camera lenses

In order to build a low cost system, commercial off-the-shelf lenses are used. Four Canon lenses with the parameters (focal length and f-number) 50 mm f/1.2, 85 mm f/1.2, 135 mm f/2.0 and 200 mm f/2.0 will be presented in the following. All of them except the 50 mm f/1.2 lens have been tested at the DLR observation site. Calculations of the point spread functions (PSF), which is the most important information for astronomical applications, show the quality of the lenses. The PSF describes the spread of a point source like a star on the sensor pixels after propagation through an imaging system. It depends on optical aberrations and light diffraction at the aperture stop.

In order to get information about the PSF the used lenses are simulated with the optical design program Zemax Optic Studio 15.5 based on the lenses patent designs.

Spot diagrams which show the geometric PSF visualize the large geometric aberrations of each lens compared to the diffraction effects. Therefore the geometric RMS radius of these diagrams

is used as image size of a point source and also for later simulations (chapter 4). Real measurements of the PSF from the available lenses are compared with the design results to see the differences between an optimal system and real measurements. As point sources the stars are used.

Especially for wide-angle space surveillance the shading of outer parts of an image is a problem as well. This effect is called vignetting and caused by the lens design. Faint objects which pass the FOV of the staring camera could disappear for the object detecting algorithm. However, there are several solutions, for example flat fielding or image processing algorithms for counter this problem which is discussed in more detail in [36].

1. Canon EF 50mm f/1.2L USM

Figure 16 shows the first analyzed lens which is the Canon EF 50mm f/1.2L USM based on the Canon patent ([37] - Patent Working Example 2). It is a Double Gauss design containing 9 lenses with a focal length of 50 mm and an aperture diameter of 41.6 mm. The rays are showing the propagation of the light through the lens system at different angles. Blue visualizes the incoming rays parallel to the optical axis and therefore vertical to the image plane. This design is optimized to a maximum half field angle of 22.71° which correlates to the red rays in the figure. Here, the vignetting of this lens can be seen, which is the strongest of the four lenses. At an angle of about two-thirds of the maximum half field are the green rays. This coloring is used for the following presented lens designs as well. Equipped with this lens the FLI PL16803 camera has a FOV of 36.4°×36.4°. For the Andor Zyla the FOV is 15.69°×18.41°.

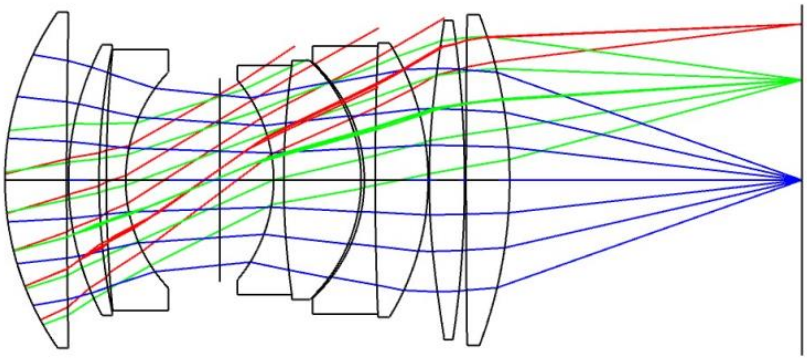

Figure 16: Canon EF 50mm f/1.2 L USM lens design.

At the center of the image plane is the root mean square (RMS) radius r_{RMS} of the spot diagram 13.07 µm, where the radius at an image height of 11 mm is 32.44 µm (figure 17). This image height is used for all following spot diagrams and results from the size of the Andor Zyla camera sensor. The colors in the spot diagrams are visualizing different wave lengths (blue= 486nm, green= 588nm, red= 656nm). However, the used cameras do not have

filters to retain the color information and the main information of the diagram is in the shape and size of the spots. Later simulations for analyzing the performance of the staring system (see chapter 4) use the PSF in pixel units PSF_P. For the FLI camera with a pixel pitch s_P of 9 µm the PSF_P would be 1.45 px at the center of the image and 3.6 px at the outer parts (see equation (3.3-1)). The Andor Zyla camera has a pixel pitch of 6.5 µm. Therefore the quantities are 2.01 px or 4.99 px. For the simulations the values valid for the center of the image are used.

$$PSF_P = \frac{r_{RMS}}{s_P} \tag{3.3-1}$$

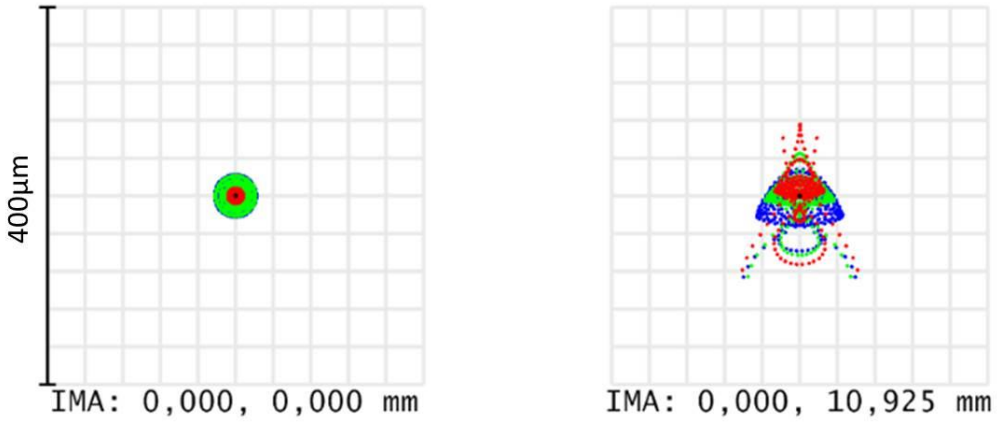

Figure 17: Spot diagram of the 50mm f/1.2 lens at the image center (left) and for an image height of 11mm (right).

The short focal length of this lens causes a low image resolution with the used cameras, which results into an insufficiently precise prediction of the location for recapture orbiting objects (shown by Monte Carlo simulations in section 5.1). Therefore the 50 mm lens is not used for surveillance and measurements but only for simulations due to the large reachable observation region.

2. Canon EF 85mm f/1.2L II USM

Another lens is the EF 85mm f/1.2 L II USM. It is also a Double Gauss design which is shown in figure 18 ([38] – Patent Working Example 1) and has an optimization for a half field angle of 14.28° (red rays). The wide angle causes also a strong vignetting in the image plane. With its focal length of 85 mm it covers an observation region of 23.45° × 23.45° attached on the FLI and 9.38° × 11.08° on the Andor camera. The aperture diameter is 70.8 mm.

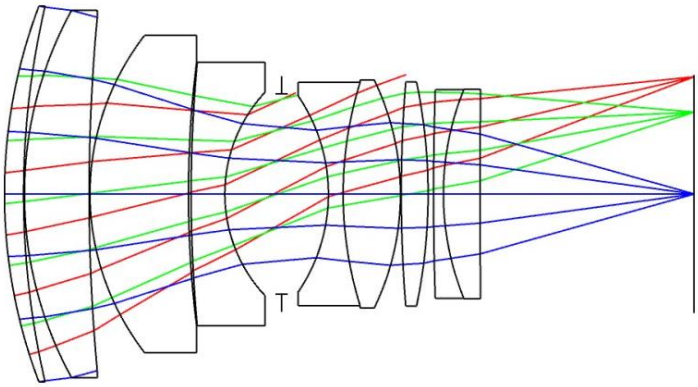

Figure 18: Canon EF 85mm f/1.2L II USM lens design.

With respect to the RMS radius of the spot diagram at the center of the image (figure 19 - top) with a value of 19.2 µm, this lens is the worst of all four. Its RMS radius increases to 22.85 µm at 11 µm image height. These quantities give simulation PSFs for the FLI camera of 2.13 px and for the Andor camera 2.95 px.

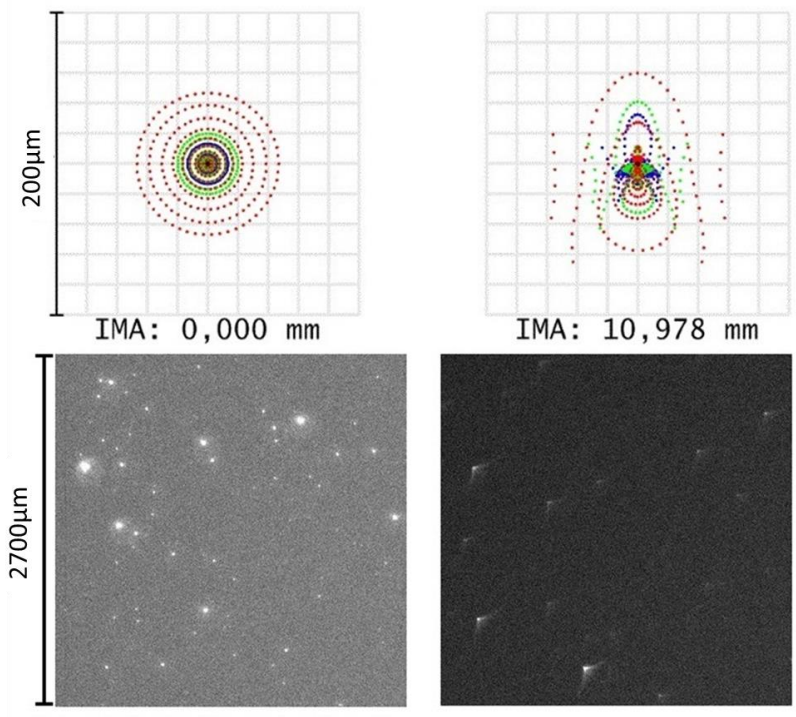

Figure 19: Spot diagram of the 85mm f/1.2 lens at the image center (left) and for an image height of 11mm (right).

At the bottom in figure 19 are shown details of an image taken with this lens equipped to the FLI camera. Measurements of the PSF of stars (which can be used as point source) give similar quantities as expected from the simulations. In the middle of the image the measured PSF is 2.52 px. The difference occurs due to the atmospheric turbulences. At the corresponding image heights the shape of the stars in the images looks very similar to the spot diagrams of the simulations.

3. Canon EF 135mm f/2L USM

The Canon EF 135mm f/2 L USM is based on a telephoto lens design which is presented in figure 20 ([38]- Patent Working Example 4). It is optimized to a half field angle of 9.22° and has an aperture of 67,5 mm. This lens has the lowest vignetting effects of the four compared lenses. Assembled to the FLI camera a FOV of 15.27°×15.27° and to the Andor of 5.94°×7.03° is achieved.

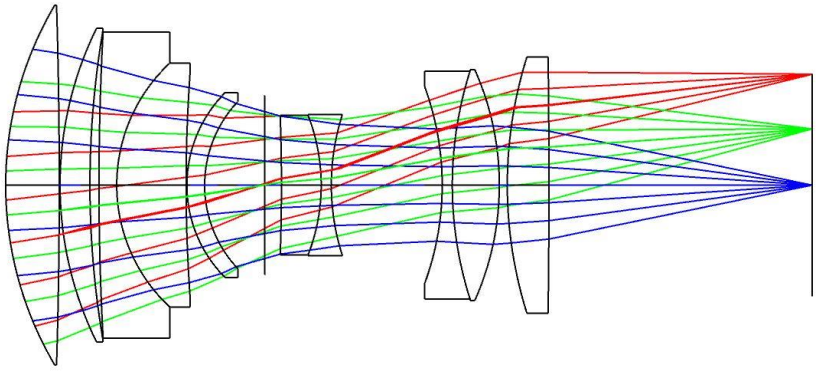

Figure 20: Canon EF 135mm f/2L USM lens design.

This lens has the best RMS radius of all lenses. According to Zemax the center of an image the radius is 7.36 µm and increases to 9.6 µm at the edge of the image (figure 21 - top). With respect of the pixel sizes PSF values of 0.82 px for the FLI camera and 1.13 px for the Andor camera are achieved. At the outer parts of the image coma is the dominant optical aberration.

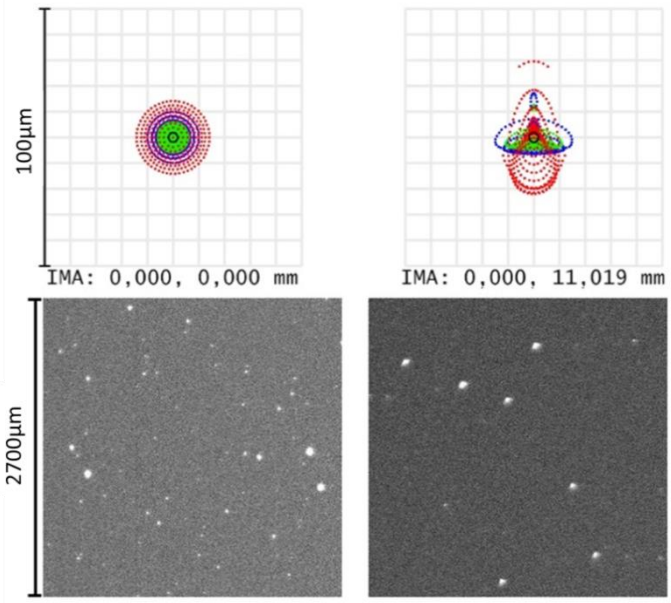

Figure 21: Spot diagram of the 135mm f/2.0 lens at the image center (left) and for an image height of 11mm (right).

As before measurements of the stars are compared to the PSF values from Zemax. Figure 21 shows at the bottom the details of an image taken with the FLI camera and the 135 mm lens.

A PSF of 1.4 px is measured for the stars at the center of the image. Again, the atmospheric turbulences cause higher PSF values than the results from the simulation.

4. Canon EF 200mm f/2L IS USM

Figure 22 shows the camera lens Canon EF 200mm f/2 L IS USM based on the Canon patent ([38] - Patent Working Example 5). Just as the 135 mm lens it is a modified telephoto design. The wide aperture diameter of 100 mm and the focal length of 200 mm are reached by using 14 lenses. It is constructed for a half field angle of 6.3 ° and has a low vignetting. Equipped to the FLI camera a FOV of 10.44 ° × 10.44 ° is and to the Andor a FOV 4.02 ° × 4.76 ° of given.

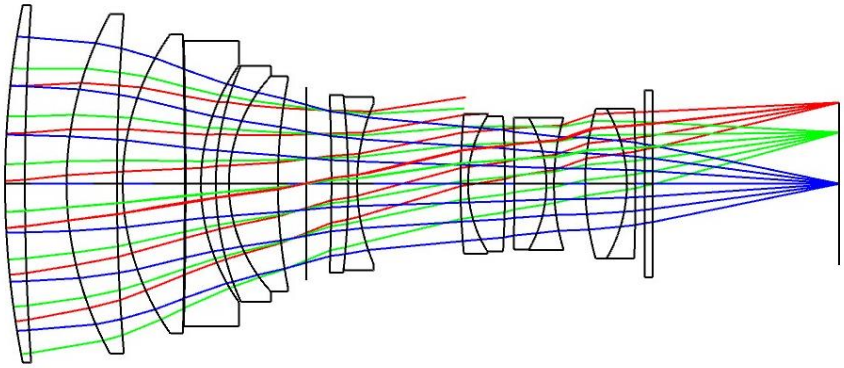

Figure 22: Canon EF 200mm f/2L IS USM lens design.

For the center of an image the RMS spot radius is 12.95 µm whereas the radius is decreasing to 11.41 µm spot radius at the image side (figure 23 at the top). Transformed into pixel of the FLI the spot has a radius of 1.44 px for the center of the image. For the Zyla camera the value is 2 px.

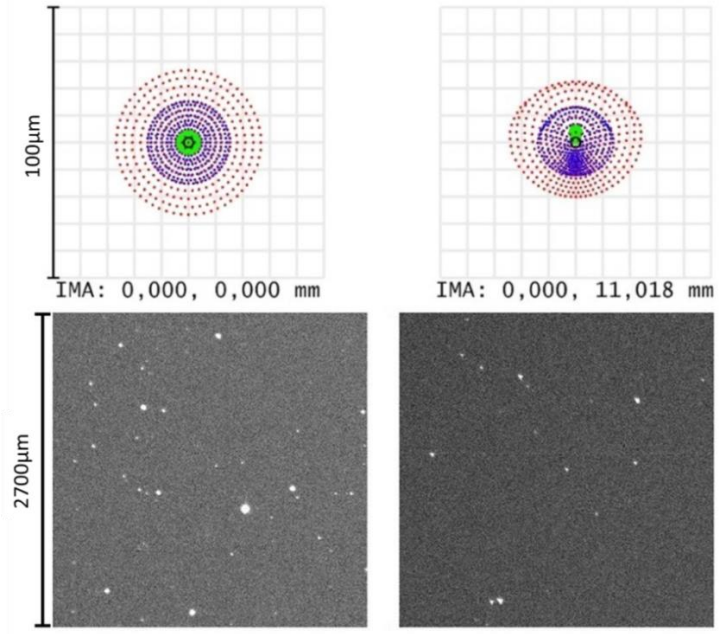

Figure 23: Spot diagram of the 200mm f/2.0 lens at the image center (left) and for an image height of 11mm (right).

Measurements with this lens and the FLI camera give a PSF value of 1.74 px at the image center shown at the bottom of figure 23.

Finally, table 3 shows a summary of all optical lens data including the PSFs which are used in chapter 4 for simulations to determine of the staring camera performances.

Table 3: Optical parameters of the presented lenses.

No. of lens	Focal length	F-number	Aperture diameter	PSF (sim. at img. center)	PSF (sim. at img. center – FLI camera)	PSF (measured at img. center – FLI camera)
1	50 mm	1.2	41.7 mm	13.07 µm	1.45 px	-
2	85 mm	1.2	70.8 mm	19.20 µm	2.13 px	2.52 px
3	135 mm	2.0	67.5 mm	7.36 µm	0.82 px	1.40 px
4	200 mm	2.0	100.0 mm	12.95 µm	1.44 px	1.74 px

In conclusion, measurements and design analyzes show the best optical performance for the 135 mm lens. These results and the wide FOV equipped to the cameras are the reasons why the recapture algorithm for chasing an RSO was tested with this lens.

3.3.4. The GPS- Timer

Exact times and synchronization between staring camera (object detection), telescope-mount and the telescope camera (recapture) is essential for a successful tracking of RSOs with predicted trajectories from the staring camera. This is accomplished with the usage of a GPS timer. For receiving the information an Adafruit Ultimate GPS receiver is used which generates a Pulse-per-Second (PPS) signal. The data processing of the PPS signal and the information of the Transistor-Transistor-Logic (TTL) in- and output of the camera are done by an Arduino Uno microcontroller. However, the accuracy of the synchronization is limited to the trigger precision of the used cameras. The time accuracy on one pixel has to be better than about 5 ms because this is the time of an RSO at an altitude of 800 km. For the Andor Zyla camera a timestamp accuracy of 25 ns is given [34]. The FLI PL16803 is limited to 40 ms due to its mechanical shutter as mentioned in subsection 3.3.2 which leads to prediction inaccuracies.

4. Technical design of a surveillance system based on PROOF simulations

The following sections describe how a passive optical staring system for space debris surveillance can be designed. Detecting objects as small as possible orbiting Earth in LEO is the major purpose of such a design. Additionally, a wide angle of the system's FOV leads to large observation regions increasing the total number of detected objects for generating or maintaining an independent database.

In the first section the simulation tool PROOF by ESA and its usage for analyzing staring system performances are presented in detail. Most important parameters and the different simulation modes are explained as well. Simulations are used to examine the detection efficiency with respect to the observation -time and -LOS of a staring system located at the DLR observation site (section 4.2 and 4.3). In section 4.4, the aperture and focal length of the camera lenses are changed to determine optimal lens parameters for a staring system. Additionally, the results show the effects of vignetting to the detection efficiency. Off-the-shelf lenses (presented in subsection 3.3.3) equipped to the staring cameras are simulated in section 4.5 and the results are discussed. Section 4.6 shows the detection efficiency for systems containing different cameras and different lenses but with similar FOVs. The performances are analyzed and a lens-camera-set-up based on the detection efficiency is suggested. In the last two sections the simulated data will be compared to real data measured at the DLR observation site and conclusions of the simulations are given.

All the PROOF simulations are based on the location of the DLR observation test site at the Uhlandshöhe in Stuttgart without any influences of weather conditions.

4.1. About the simulation software PROOF

Space debris models like MASTER (Meteoroid and Space Debris Terrestrial Environment Reference) from ESA [39] describe the space debris situation in LEO to GEO. In order to get a link to measurements from observation campaigns and for validation of such models, the Technical University of Braunschweig developed the simulation software PROOF. This software tool gives forecasts about pass characteristics of the space debris population for given sensor characteristics [40]. As observation facility radar and ground or space based optical systems are possible. RSO passing rates of the chosen FOV are transformed into detection rates by mathematical methods based on sensor specific parameters of the system. The major tasks of PROOF are validation of space debris models, analysis of measurement data and planning of observation campaigns. For the following simulations the PROOF version from 2009 is used.

The necessary PROOF parameters are sorted in five categories. First, there are the basic settings, where the observation time and duration can be adjusted.

The second category contains the analysis mode settings, where a statistical, a deterministic and a hybrid mode can be selected. For the following simulations the statistical mode based on the MASTER space population is used due to the random distribution of RSOs passing the FOV and the availability of objects smaller than 10 cm. The deterministic mode, where TLEs can be loaded and the hybrid mode, which is a mixture between both modes are not used because of the missing geometric sizes of the objects and will not be explained further more. Choosing the statistical mode allows adjusting some statistical parameters. These are for example the number of Monte Carlo runs, the number of simulation steps per object or the upper and lower threshold diameter of the objects.

The next category is for the operational mode settings. At first it must be chosen, if the surveillance is ground based or orbit based. For a ground based observation site, which is used for the following simulations, the settings contain information about the location of the observation site and the observation itself. It consists for example of the observation range and the information about the LOS. The LOS depends on the system's mount. It can be a fixed pointing of the camera (azimuth and elevation) or the pointing changes with the rotation of Earth (right ascension and declination).

In the fourth category the sensor mode settings are contained, which includes the possibility to choose a telescope or radar based surveillance. Parameters from the optical sensor and the optical system can be adjusted, if the telescope settings are chosen. The main parameters are the diameter of aperture, FOV, number of pixels per row, pixel size, pixel scale, exposure time, gap time between the frames, threshold parameter for detection and the PSF of a point source in pixel units which was examined in subsection 3.3.3. It is possible to adjust the readout- and dark-noise of the optical sensor. A file with the quantum efficiency of the optical sensor and the transmission spectrum of the atmosphere can be loaded as well.

The last category is for the plot options, where the plots for analyzing the data can be adjusted. This category is not used due to data processing after the simulations and is therefore not explained in more detail. Table 4 shows the most important settings for the following simulations.

Table 4: PROOF simulation parameters.

Parameter	Value
Observation date	2013.04.01 – 2013.04.10 2014.04.01 – 2014.04.10 2015.04.01 – 2015.04.10
Duration	11 h per day
Min. object size	0.1 m
Max. object size	100 m
Min. range	200 km
Max. range	4000 km
Geodetic latitude	48.78253 °
Geodetic longitude	9.19641 °
Geodetic altitude	355 m
Azimuth	0 °
Elevation	90 °
Diameter of Aperture	Lens dependent
FOV	System dependent
Number of pixels per row	Camera dependent
Pixel size	Camera dependent
Pixel FOV	System dependent
Exposure time	1 s
Gap time	Camera dependent
PSF	System dependent
Threshold parameter	2
Readout noise	Camera dependent
Dark noise	Camera dependent

However, aberrations of the optical system, vignetting or influences due to weather conditions have no effect on the simulation results. Vignetting affects the performance the same way as decreasing the FOV of the system which is shown in table 6 in section 4.4.

4.2. Determination of the observation time

Passive optical observation is strongly dependent on light conditions. The Sun has to be at a specific altitude region that neither the ambient light is too bright at the observation site nor the orbital objects are in Earth's shadow. This dependence on light conditions and the tilt of the Earth causes a changing observation time all over the year.

Staring systems pointing in direction zenith are simulated for analysis of the observation times. In figure 24 the detection efficiency of three different months during a year are presented to visualize the seasonal variation of observation times. The detection efficiency shows the percentage of detected objects with a system set-up containing the Andor Zyla camera and the 135 mm f/2 lens (FOV = 7.0 ° × 5.9 °) with respect to the total number of passed RSOs. For compensating the statistical errors a Gaussian filter was used to smooth the curves. The Sun's altitude is depicted by the dotted line to show the correlation to the detection rate of the illuminated objects.

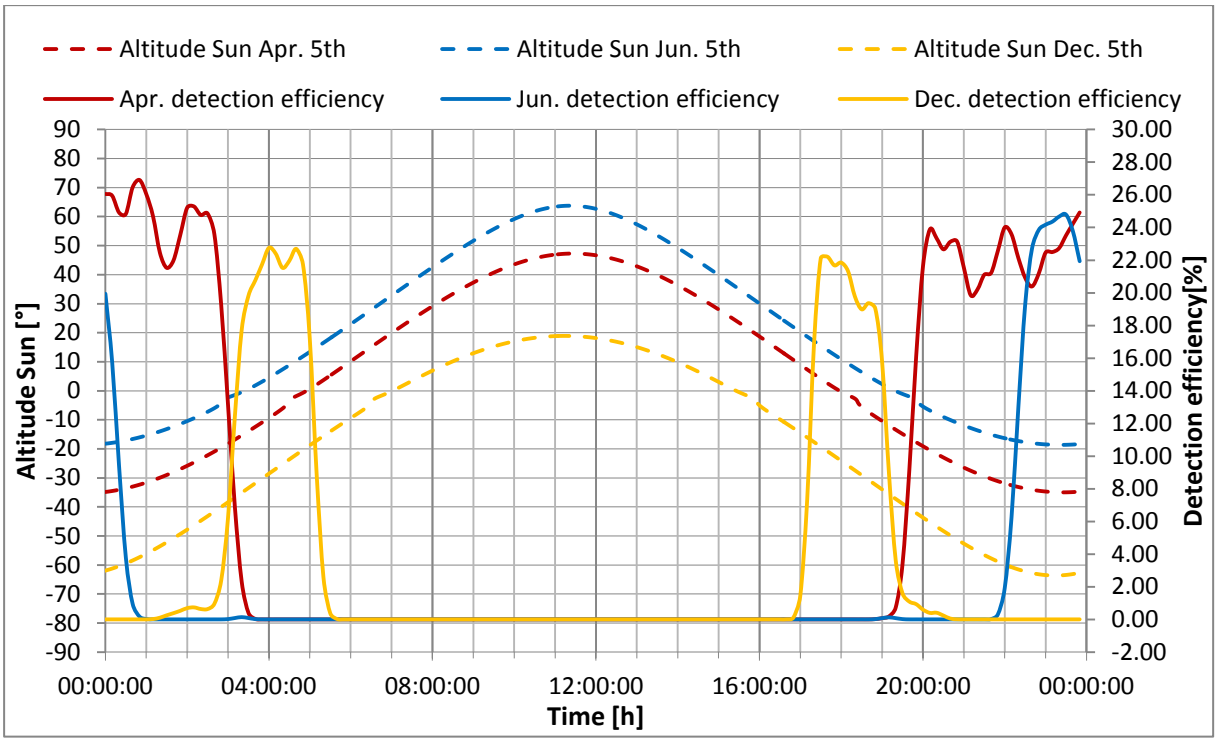

Figure 24: Detection efficiency for different month during a year compared to the suns altitude (dotted).

All over the year the possible observation time starts about one and a half hours after sunset and ends about one and a half hours before sunrise. This depends on the Sun's altitude and therefore the ambient light at the observation site which disturbs the optical sensor. Since the Sun is below an altitude of -15° the ambient light level is sufficiently low for detecting RSOs with this staring system. From October until March the sun reaches altitude levels below about 40° beneath horizon. Most LEO objects are shaded by Earth if that is the case. The missing illumination leads to a decreasing of the detection efficiency to almost 0 % at these times. RSOs on higher altitudes than LEO are still illuminated and can be detected. During the months from April until September all-night observations are possible. Because of shorter durations between sunset and sunrise the observation time decreases until the months of June and July where the time is the shortest. The low maximum of the detection efficiency is caused by small RSOs which cannot be detected by the system.

These simulations are the base for the determination of the optimal observation time. For comparisons of different system parameters a specific observation time must be chosen. April and September are the most favorable months due to the long observation possibility and the duration from sunset to sun rise is about 11 h. Directly after sunset and before sun rise occurs the gap mentioned before, where no objects are detected because of the ambient light. So the maximum detection efficiency is decreased for all further simulations. However, this is does not matter for a direct comparison of systems.

4.3. Determination of the line of sight (LOS)

Additionally, the observation time depends from the LOS. If the optical system is not pointed directly onto zenith, the observation times are different to those which were discussed before. These effects are shown in figure 25 based on simulations for a LOS with different elevations, going down from zenith to 15° above horizon. As an observation epoch December is chosen and a pointing directed to an azimuth of 270°. Figure 25 shows the number of detected objects as a function of the time for different LOS elevations.

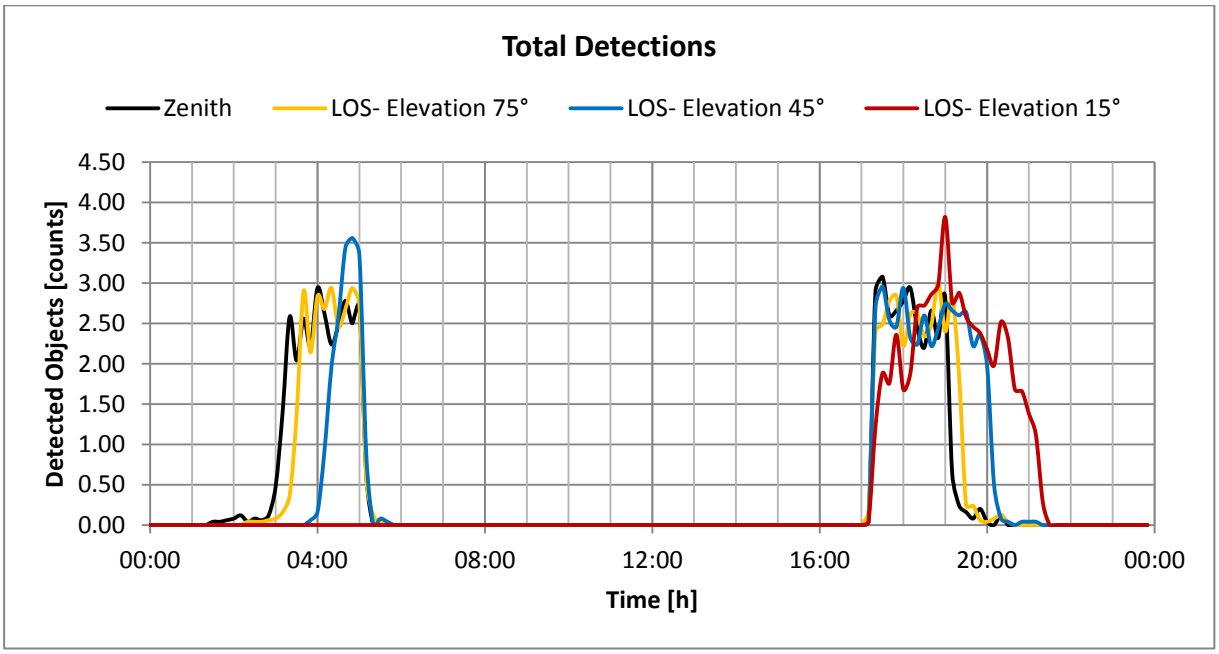

Figure 25: Total detected objects for different line of sight elevations averaged in December.

The total number of detections is similar for different elevations, but the time is shifting for a possible detection of an RSO. During the morning the time span for an observation is getting narrower the lower the elevation of the LOS is. At an elevation beneath 15° no detections are possible any more. The orbiting objects are longer in Earth's shadow and therefore the begin of an observation shifts to later times. However, the time where the ambient light at the observation site is too bright (falling edge in figure 25) is consistent. For observations in the evening the rising edge keeps the same but the duration for an observation is extended. The LOS pointing to West where the Sun sets leads to a longer illumination of the RSOs in the LOS.

Changing the elevation also has other effects to the system. Comparing figure 25 to figure 26 shows the similarity of the shape of the curves for total detections and detection efficiency. However, the latter one decreases the closer the LOS is pointing onto the horizon. This effect occurs much more during evening observations.

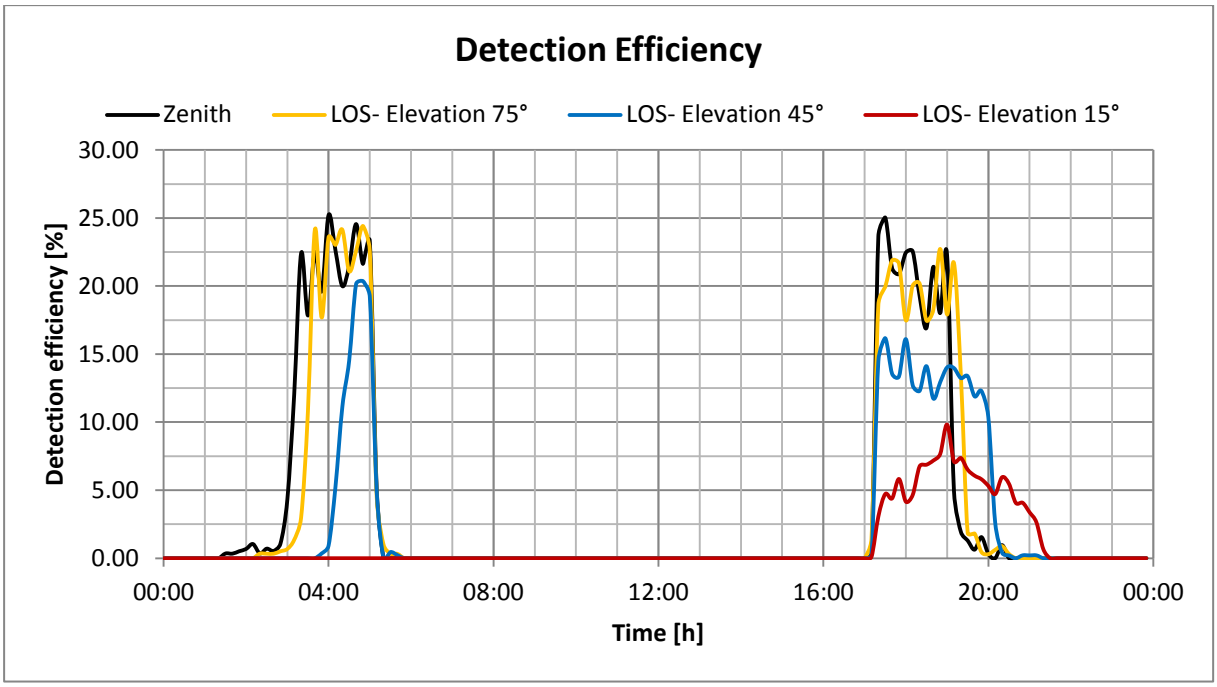

Figure 26: Detection efficiency for different line of sight elevations in direction West.

There are some reasons why this can happen. One reason is the longer distance to the targets caused by the angle. This causes a loss of light because of the increased distance itself but also due to the longer path through the atmosphere which absorbs and scatters the light or distorts the signal because of turbulences. However, this reason has the same effects for morning and evening observations. Second, in the evening the western sky is much brighter due to scattered light in the atmosphere from the setting Sun. This leads to an increased threshold level for detection brightness and therefore the RSOs have to be brighter for a successful detection.

Shown before in figure 25 the total number of detections is still the same but nevertheless the detection possibility is decreasing. This is caused by the increasing number of passing objects in the FOV the closer the LOS is getting to horizon.

An adjustable Staring system could extend the surveillance time of an observation site for the months from October until March. The elevation and orientation of the LOS has to be adjusted to the night time. It begins orientated to zenith after sunset and moves into West when the objects disappear due to Earth's shadow. The system has to change its orientation to a low Eastern elevation when the last objects are not illuminated any more even for a low Western elevation. For getting a better detection efficiency the system should point towards zenith as long as possible in the evening and as soon as possible in the morning. During the months April until September the pointing can be towards zenith due to the constant illumination.

A calculation based on RSOs in the TLE database led to the total number of objects passing the FOV for different elevations and azimuths. Moving the pointing of the camera system to low elevations for one specific azimuth increases the number of TLE objects in the LOS (see table 5).

This is caused by the projection of the camera's FOV on the sky. The closer the alignment of the camera to horizon the larger is the observed area. Resulting numbers in the calculations are not affected by any optical conditions except the FOV.

Table 5: Total FOV-passing objects for different line of sights.

Elevation	North	East	South	West
10°	7615	5527	3281	5491
20°	5109	4019	2721	4037
30°	3215	2824	2190	2873
40°	2317	2180	1759	2205
50°	1827	1867	1481	1766
60°	1527	1581	1304	1543
70°	1437	1396	1245	1387
80°	1280	1271	1226	1283

Many RSOs have pole synchronized orbits which result in the highest number of objects passing the FOV in direction north for the northern hemisphere and south for the southern hemisphere. Based on the TLE catalog (01.04.2016) in table 5 are shown the passing numbers of a FOV of 5.9° (corresponding Andor Zyla camera & 135mm camera lens) for different cardinal directions with the origin at the DLR observation site for an observation period of one day

4.4. Aperture VS Focal length

Section 3.2 shows the dependency of the received light of an RSO from the focal length and the aperture diameter in theory. In order to verify these results 41 simulations are done for different camera lens specifications. The focal length was varied from of 25 mm to 200 mm in steps of 25 mm and for each focal length the aperture diameter was changed in the range from 20 mm to 140 mm in steps of 20 mm. Systems with f- numbers much smaller than one are too difficult to manufacture. Therefore the simulations for small f-numbers are neglected.

As observation parameters a LOS towards zenith from the coordinates of the DLR observation site and the specifications from the Andor Zyla camera are used. The observation times are 30 days in April from sunset until sunrise (11h). April was chosen because of the possibility for long observations during the whole night as mentioned in section 4.2.

Table 6 shows the detection efficiency per hour of the different system set-ups. For an increasing detection efficiency the aperture diameter has to increase due to the correlation to the collected light. The more light of an object is received the higher is the system's efficiency. However, an increasing focal length results in a decreasing detection efficiency because of the faster movement of the RSO on the camera sensor. This leads to less light on a receiving sensor pixel. These results are matching to the theoretical results from section 3.2.

Table 6: Detection efficiency for 330h of observation during April with an Andor Zyla camera and lenses with different parameters.

Aperture diam. \ Focal length	25mm	50mm	75mm	100mm	125mm	150mm	175mm	200mm
20mm	5.26	4.87	4.66	4.29	4.03	3.80	3.75	3.64
40mm	7.37	7.00	6.82	6.59	6.20	6.02	5.60	5.29
60mm	-	8.39	8.23	8.02	7.71	7.53	7.29	7.03
80mm	-	-	9.27	9.04	8.77	8.55	8.37	8.36
100mm	-	-	-	10.00	9.67	9.30	9.20	9.11
120mm	-	-	-	-	10.57	10.29	10.11	10.05
140mm	-	-	-	-	-	11.13	10.98	10.87

In figure 27 the detection efficiency as function of the object size is shown. The focal length of the equipped lens is set to 200 mm and the aperture diameter is changed. As camera the Andor Zyla is chosen for the simulations. Minimum detectable object sizes are getting smaller the more the aperture diameter is increasing. Small objects reflect less light than bigger ones of the same materials and the sensor has to be more sensitive or the lens has to collect more light for a successful detection. The maximum detection efficiency is achieved with apertures larger than 100 mm in diameter for object sizes of about 0.8 m while for smaller apertures larger objects are necessary to reach the maximum. A saturation of the detection efficiency begins at the maximum and remains for larger object sizes. Statistic errors cause long error bars for RSOs larger than 10 m because the low numbers of objects of these sizes. A possible reason why the detection efficiency is not continuously increasing for very large RSOs is explained in section 4.5.

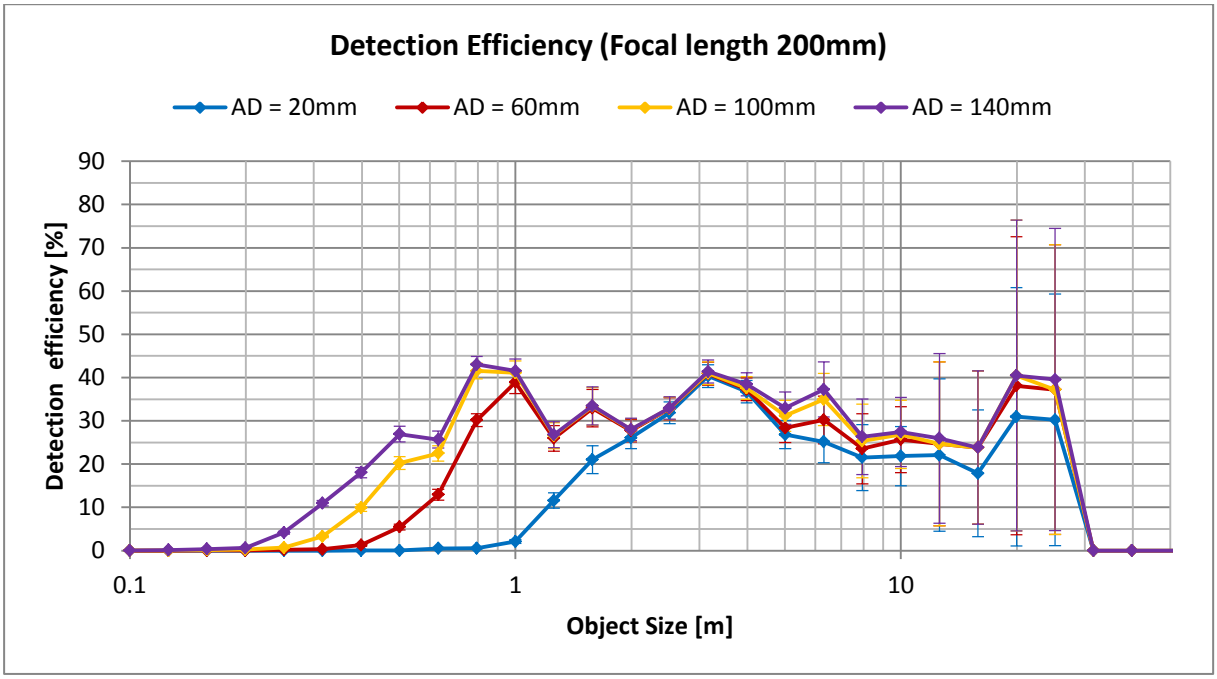

Figure 27: Detection efficiency for 330h of observation during April with an Andor Zyla camera and a lens with focal length of 200mm and different aperture diameters.

Figure 28 visualizes the results of simulations for a fixed aperture diameter and changing focal lengths. As mentioned before a short focal length has the advantage that the object moves slow on the sensor chip of the camera. However, the effect has not as much influence as a change in the aperture diameter (see also equation (3.2-7)). The minimum detectable object size keeps almost the same but the possibility of a detection increases more than 20 % for objects at sizes of about 1 m. This improvement of the performance can be very important for space surveillance due to the high number of objects in this size. More incoming light of larger RSOs saturate the pixels fast enough even for longer focal lengths. Therefore the curves become more similar for increased object sizes.

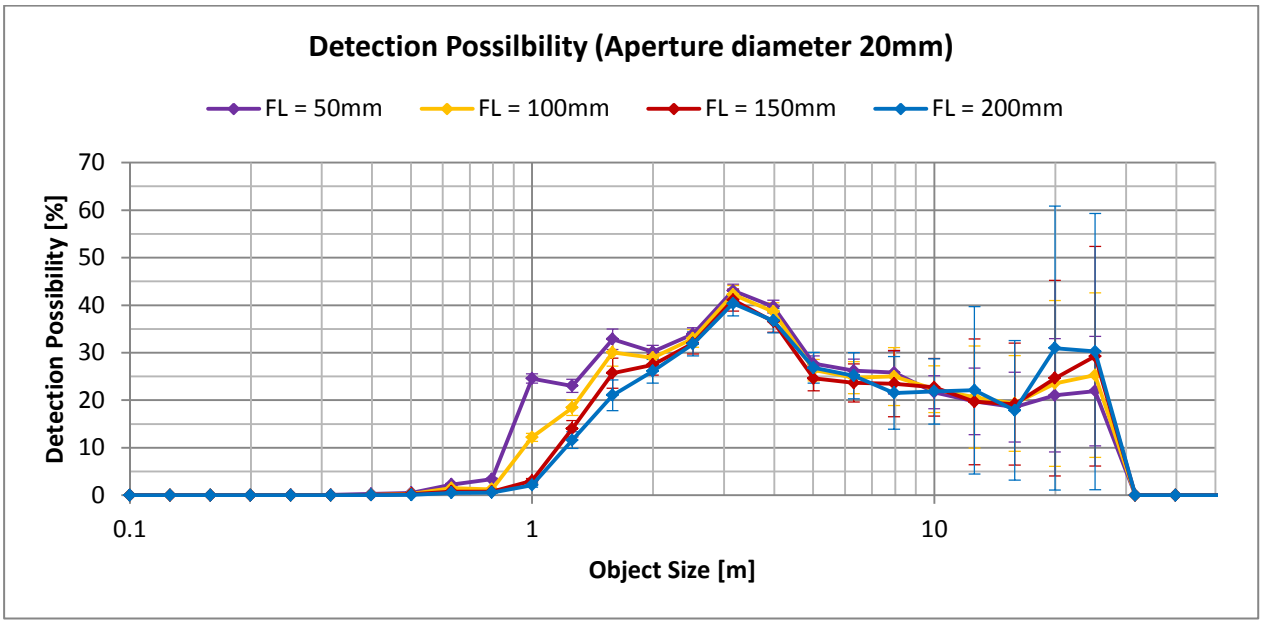

Figure 28: Detection efficiency for 330h of observation during April with an Andor Zyla camera and a lens with aperture diameter of 20mm and different focal lengths.

The simulations are verifying the calculations from section 3.2. A large aperture diameter effects more the detection efficiency than the focal length (see table 6). These results are based on simulations of lenses which are not commercially available and are just showing the effects which apertures and focal lengths have to systems for detecting RSOs. Commercial off-the-shelf lenses are simulated in the following sections.

4.5. Simulations of various off-the-shelf lenses equipped to the staring camera

After validation of the important camera lens parameters the commercially off-the-shelf lenses presented in subsection 3.3.3 are discussed. These lenses are cheaper than specific designs due to mass production, which is important for a low cost system.

As before 30 nights in April with observation durations of 11 h are chosen for these simulations. The pointing of the system is towards zenith and the weather conditions are not considered. As camera the Andor Zyla is used for all simulations to have comparable results.

At first the detection efficiency is analyzed to give an overview of the performances of the different lenses. Of course a short focal length and a wide aperture is still the best solution but these lenses differ in both and additionally in their imaging quality given by the PSF (see table 3). However, the detection efficiency is not the only important number for a space surveillance system. For initial detection of space debris the quantity of total detections is important as well. This number correlates with the FOV of the system and is analyzed later on.

1. Detection efficiency

Figure 29 shows the very different results of five camera lenses. Despite the longest focal length the Canon 400 mm lens seems to be the best choice in respect of detection efficiency, especially for small RSOs. This comes from the wide aperture of almost 143 mm. Comparing the 135 mm and the 85 mm shows the higher influence of a wider aperture and a shorter focal length than the PSF. Therefore the 85 mm lens shows better performance.

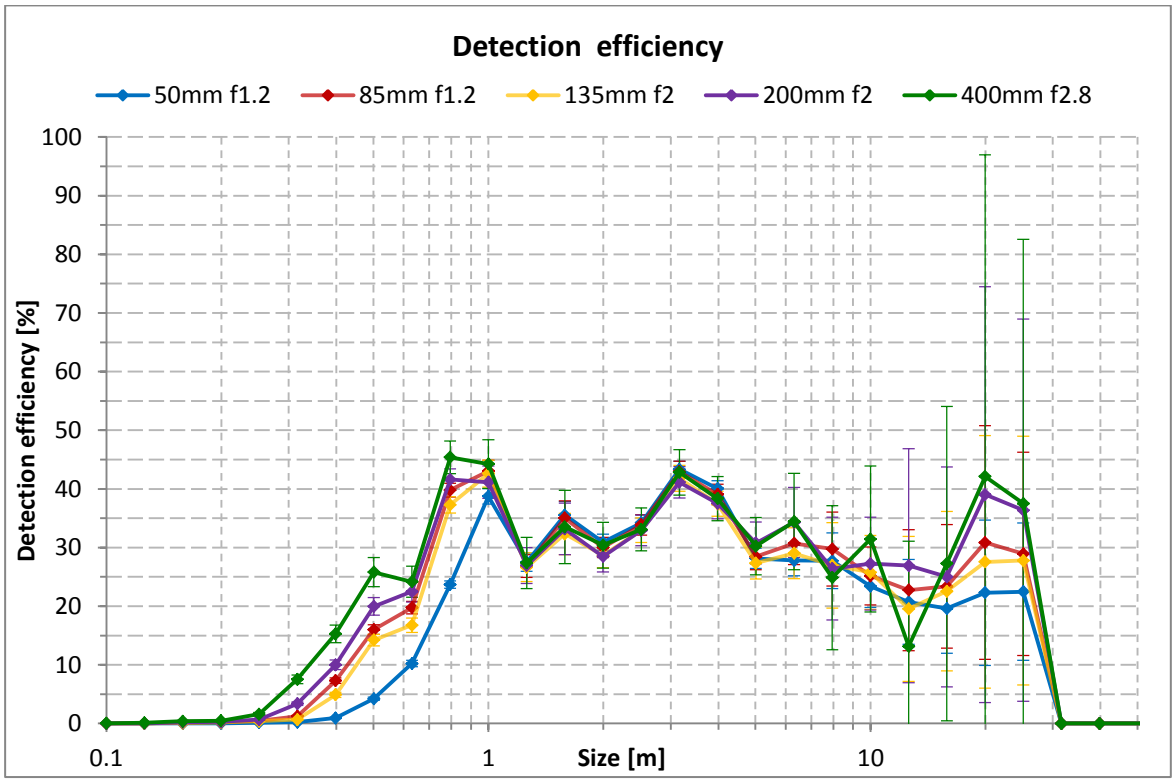

Figure 29: Detection efficiency for a system consisting of an Andor Zyla camera and different lenses.

The error bars from the statistical error are increasing with a longer focal length. This results from the correlating smaller FOV and therefore from the decreasing number of passing RSOs.

As mentioned in the section before, it might surprise that the detection efficiency is not continuously increasing for larger objects. Instead of that the efficiency decreases. A possible reason is shown in figure 30 and is explained in the following. It visualizes the altitude

distribution of the LEO objects. In four subplots the objects are sorted additionally by their size. The histograms are drawn with the simulation data from PROOF based on the MASTER model and might be different to the TLE catalog. This allows the additional drawing of the detected objects of the Andor Zyla camera and the 135 mm camera lens (yellow).

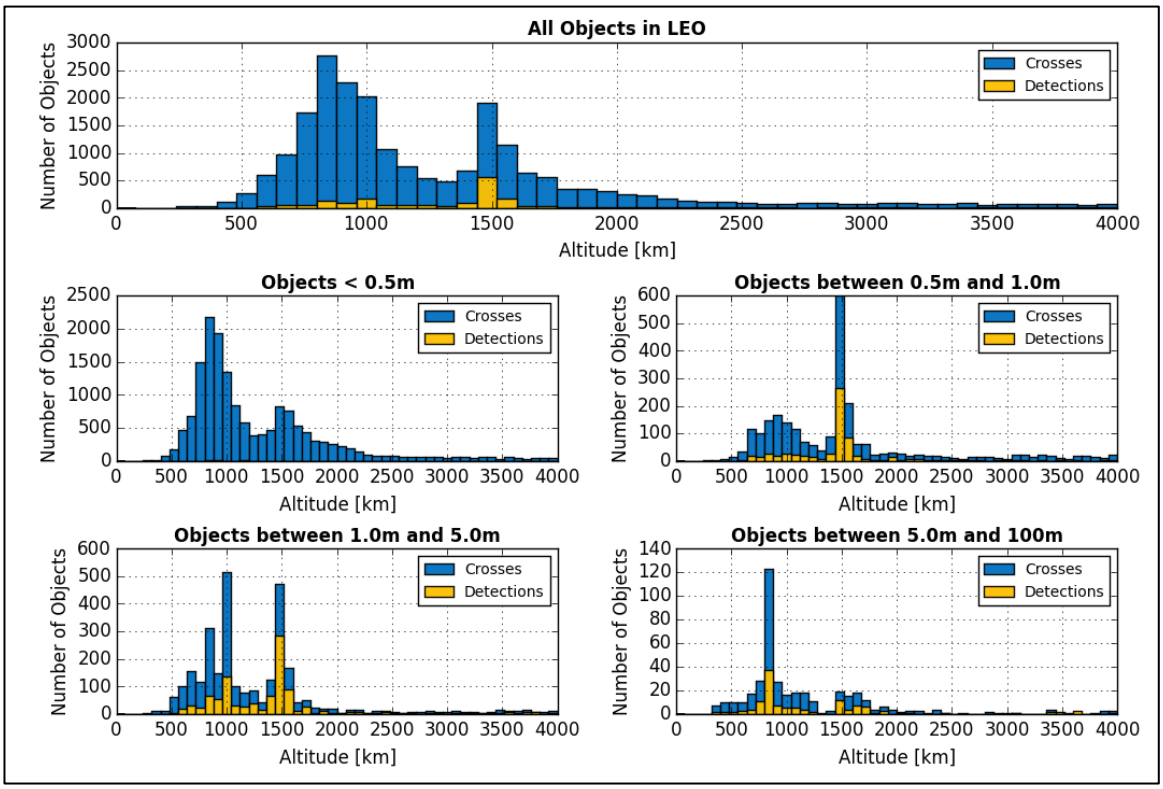

Figure 30: Number of FOV- crossed (blue) and detected (yellow) objects relating to their altitude. Subplots are showing the distribution separated for different object sizes.

Figure 30 shows the higher possibility for a detection of an object at higher altitudes (1400km) than a detection on lower altitudes (800km). This results from the corresponding velocities of the RSOs (equation (3.2-2) in section 3.2). High and therefore slow RSOs exposure the sensor pixels longer than lower ones. According to the subplot containing the object sizes ranging from 5 m to 100 m (bottom/right) most large LEO objects are orbiting Earth at lower altitudes (lower than 1000 km). Therefore the angular velocity is fast and even with more reflected light from the sun the sensor pixels are not exposed enough. The efficiency decreases for RSOs larger than 4 m in all PROOF simulations which are showing the detection efficiencies due to this. However, this pattern does not occur in real measurements (see section 4.7)

2. Total detections of RSOs

The total detections per hour of a surveillance system with the same parameters as before are shown in figure 31. This number depends mostly on the FOV of the optical system due to the corresponding number of RSOs passing the FOV.

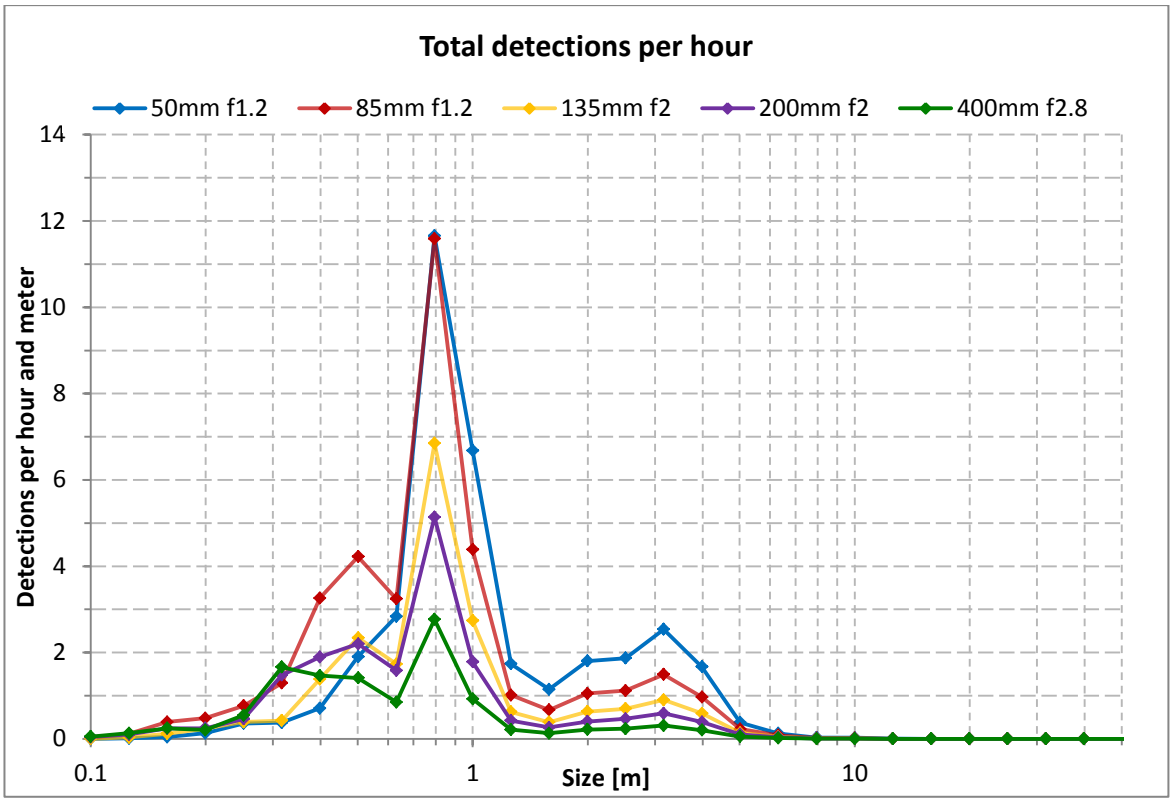

Figure 31: Total detections per hour for a system consisting of an Andor Zyla camera and different Canon camera lenses.

A decreasing focal length causes an increasing FOV. Therefore, the 50 mm lens shows most detections per hour for objects larger than 60 cm diameter. For smaller objects the aperture diameter has still a bigger influence. Much more objects are passing the FOV of the 50 mm lens but only few of them are detected by the system. In this regime the 85 mm lens gives the best results due to a good combination of FOV and detection efficiency. The small number of detections for sizes larger 1 m is due to the very few orbiting objects with this size. Hence, the small number of detections for small objects is caused by the low detection efficiency of such systems. In figure 32 the number of detections per hour is integrated beginning from small objects. This shows the absolute number of detected RSOs for specific sizes based on the used camera lens. A Zyla camera equipped with the 50 mm lens could detect almost 13 objects in one hour in total. However, the narrow FOV of the 400 mm lens leads to just two detections per hour which is too less for a system for initial detection of RSOs. As mentioned before just few objects larger than 10 m are orbiting Earth, which causes a saturation at this region for all lenses.

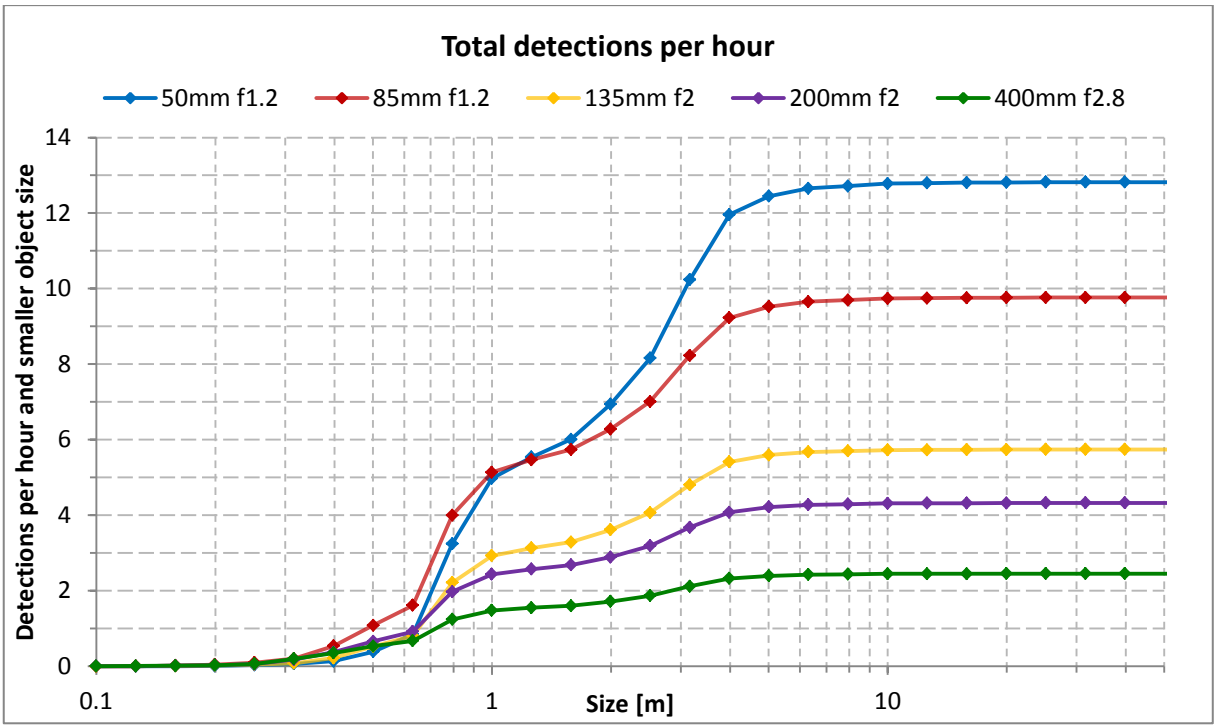

Figure 32: Integrated numbers of total detections per hour for a system consisting of an Andor Zyla camera and different Canon camera lenses.

Based on these simulations the Canon 85 mm lens is a good choice as Staring Camera lens if the Andor Zyla camera is used. Despite its short focal length with the advantage of a wide FOV it has a wide aperture diameter of 70.8 mm. Large numbers of total detections allow using such systems as surveillance system for initial object detection.

4.6. Comparison of systems with similar FOVs

As shown in the section before, the FOV is a very important parameter for initial detection of RSOs. Therefore, it should be as wide as possible. This angle depends in addition to the focal length of the lens f' to the camera sensor size d_s. The correlation is shown in equation (4.6-1):

$$FOV = 2 \cdot \tan^{-1}\left(\frac{d_s}{2 \cdot f}\right). \qquad (4.6\text{-}1)$$

Two different sensor sizes of the presented cameras allow comparing the performances of systems which are set up differently but having similar FOVs. A FOV of 9.38° per side for a square shaped sensor is given by the Andor Zyla camera equipped to the 85 mm lens which is according to the sections before a good solution for space surveillance. 10.44° is the FOV of the 200 mm lens attached to the FLI PL16830 camera. As third possibility a CMOS sensor named CMOSIS CMV4000 is used as low cost solution. Its FOV covers the largest angle of 12.7° using the 50 mm lens. An overview of the system FOVs is given in table 7 at the end of this section. Readout noise and dark noise (table 2) has to be adjusted for using different cameras. The gap

time between two images of the series is changing as well. The FLI camera for example has a much longer readout time because of its CCD sensor and therefore a longer gap time (4s) has to be used compared to the Andor camera (2s). For the CMOSIS CMV4000 the same parameters are used as for the Andor Zyla camera because of the similarity. The results of the simulations are shown in figure 33.

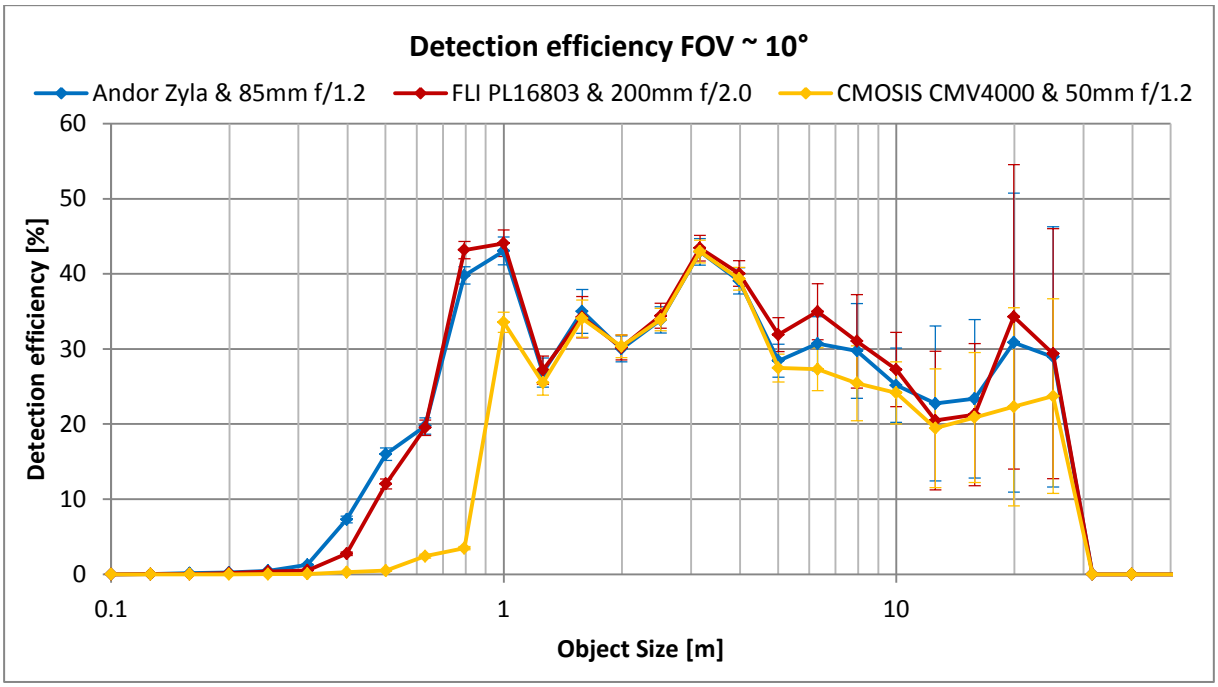

Figure 33: Detection possibility for three different "staring" systems with field of views of about 10°.

Despite the wider aperture of the 200 mm lens the Andor camera with the 85 mm lens gives slightly better results in respect to detection efficiency of small objects. However for object sizes larger than 60 cm the FLI camera equipped with the 200 mm Canon lens is the better solution. The CMOS sensor achieves very bad results for all sizes which can be caused due to its small pixel size of 5.5 µm and sensor size (11.3 mm × 11.3 mm). In order to achieve the FOV it has to be equipped with the 50 mm lens which has the smallest aperture. In conclusion the results show a similar performance of the Andor Zyla camera and the FLI PL16803 with their corresponding lenses as surveillance system. Both set-ups are suitable for this kind of task.

It is possible to extend the covered region of the sky with other combinations of lenses and cameras but this is at the cost of the performance. Figure 34 presents the systems with FOVs of about 15.5°. In order to show the loss in detection efficiency the FLI camera with the 200 mm lens from figure 33 is added as reference (black). The exact FOV angles are 15.68° for the Andor camera, 15.27° for the FLI camera and as before 12.7° for the CMOS sensor chip.

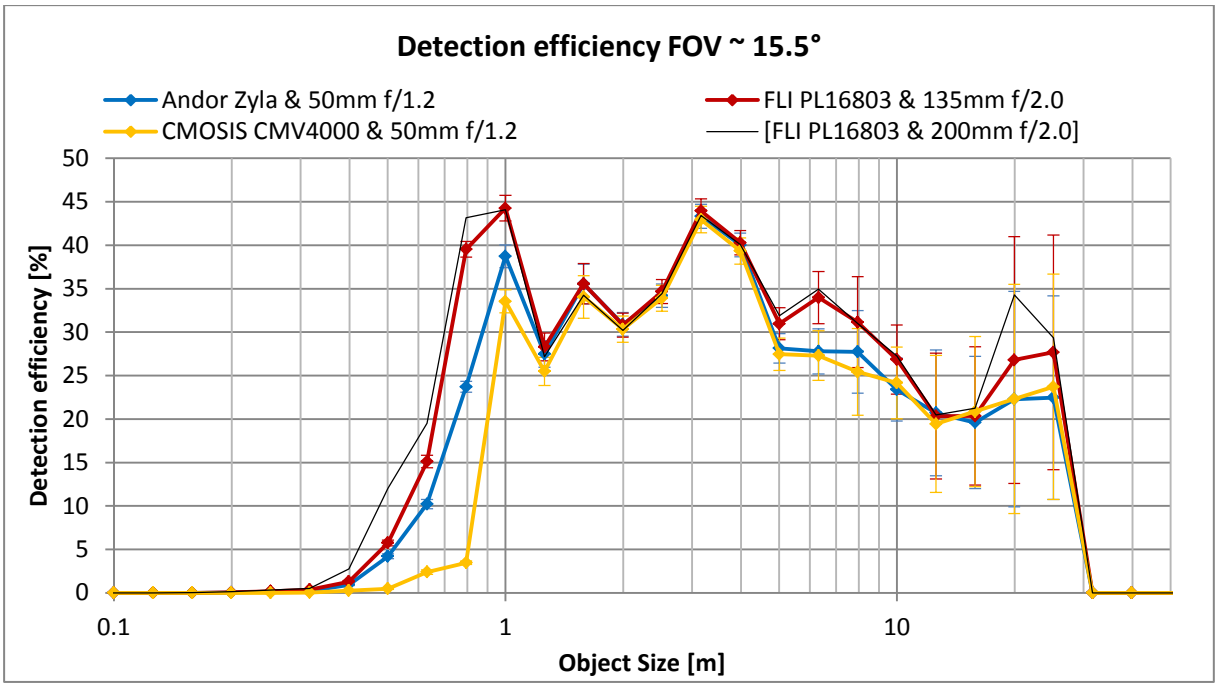

Figure 34: Detection possibility for three different "staring" systems with field of views of about 15.5°.

The best solution for FOVs of about 15.5° × 15.5° is the FLI camera equipped to the 135 mm lens (red) due to the wider aperture. Compared to the results of the 200 mm lens attached to the FLI camera (figure 33) the efficiency is just slightly less performant for small RSOs. For objects larger than 1 m the curves are almost identical. However, it increases the FOV by a factor of about 1.5 and leads to a gain in total detections.

Table 7 shows the exact FOVs of the two cameras equipped with the lenses used for the simulations for giving an overview. Additionally, systems with FOVs of about 5.5° are included for which a set-up would be possible with the presented components. However, performance analyzes are not shown due to the small FOV and therefore few passing RSOs.

Table 7: Different FOVs for the camera system.

FOV	Camera	Focal length
5.94°	Andor Zyla	135mm
5.27°	FLI PL16803	400mm
9.38°	Andor Zyla	85mm
10.44°	FLI PL16803	200mm
15.68°	Andor Zyla	50mm
15.27°	FLI PL16803	135mm

In conclusion, it can be claimed that the combination of the FLI PL16803 and the 135 mm lens would be a good staring system for space surveillance. Its large FOV compensates the weakness for detecting small objects. If the focus is on detecting small objects the Andor Zyla camera should be equipped with the 200 mm or the 400 mm lens (see figure 29 in the section before).

4.7. Comparison of the simulations with real detected data

Analyses of the performance were done for different staring system set-ups. Due to the lack of information about the geometric shape of the LEO objects the size information is based on the RCS, available for TLE-objects in SATCAT.

The RCS is the size of a reflecting area which has the same radar echo as the target for investigation. It is with respect to orbiting objects mainly measured by the phased array radar station in Eglin, Florida (figure 9, [28]). High fluctuations in the quantities of the RCS are observed for example due to the tumbling motion of the objects or corner specular reflections. Therefore averaging is needed to smooth the object sizes. These averaged object sizes are the RCSs contained in the SATCAT. However an easy transformation from RCS to the geometric shape is not possible because of the dependence of the RCS to the objects material. Therefore, the following analysis is based on the RCS. Relations from RCS to the geometric shape can be found in reference [28].

Three observation campaigns with a total observation time of 11h in July 2016 were done for a system set-up of the Andor Zyla camera equipped with the 200mm f/2.0 lens. The measurements are compared with TLE data for the same observation conditions and are shown in figure 35. Furthermore, it shows the calculated detection efficiency of this data.

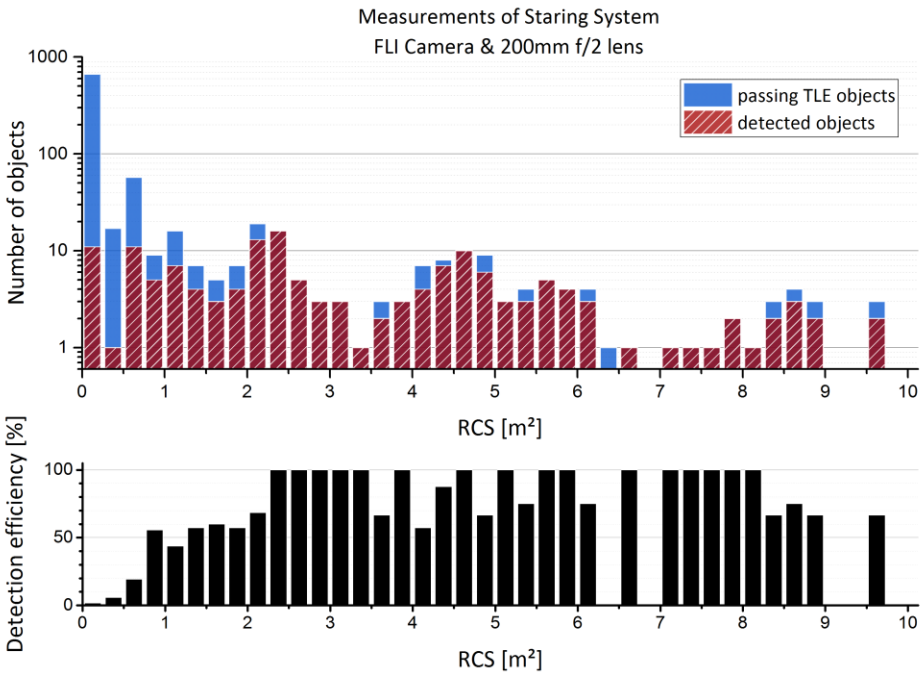

Figure 35: Measurements compared with computer based information of TLE objects passing the FOV of the staring system (Andor Zyla camera & 200 mm f/2 lens) separated into object size (Above). Detection possibility of the measurements from above (Bottom)

This system is able to detect RSOs in LEO with radar cross sections of all sizes despite the low detection efficiency for small objects. For radar cross sections above 0.75 m^2, the detection

efficiency becomes greater than 50 %. In contrast to the simulations, real measurements show that the detection efficiency does not drop for RSOs larger than 2 m^2. The used gap time of 10 s between two images caused undetected crosses of RSOs. Therefore wells in the detection efficiency occur in figure 35.

During the observation, 199 objects passed through the FOV of the system in total. 157 RSOs are contained in the TLE database. 42 detected objects (21 %) have no corresponding entry and are not included in the analysis due to the missing information about the size. PROOF simulations are predicting 141 (±12) detections for the same parameters. With respect to the outdated space population model from 2009 used by PROOF and the increased number of RSOs (approx. 15 % since 2009), a similarity for the numbers of detections can be seen. Previous measurements based on the FLI PL16803 camera equipped with the 135 mm f/2.0 lens are showing a similar agreement [41].

4.8. Conclusions of the simulations

The differences in observation time, direction and set-up are shown by the simulations with PROOF. It can be assumed that the best observation time for the presented system starts about 1.5 h after sunset and ends 1.5 h before sun rise. During winter a gap occurs where no LEO objects can be detected due to objects in Earth's shadow. Despite the lower numbers of passing RSOs a system should be set up towards zenith where the detection efficiency is highest.

Calculations as well as simulations showed that the camera lens should have a short focal length and a wide aperture. A combination of the FLI PL16803 camera and the 135 mm f/2.0 lens with its large FOV is a well performing system for space surveillance. A system set-up with the Andor Zyla camera and the 400 mm f/2.8 or 200 mm f/2.0 lens is suggested at the expense of a smaller FOV if the primary aim is on detecting small and therefore faint objects. The smaller FOV could be compensated by a multi staring system where more than one camera can be connected to cover a larger region.

Comparing the simulation with real measurements shows differences in respect of the detectable object size. According to PROOF the detection efficiency of large objects is decreasing after the maximum at about 1 m. However, real measurements reach maximum efficiencies of 100 % without drop at larger sizes. For smaller sizes a comparison is difficult due to the differences of RCS and geometric size. However, the simulations shown how the camera lenses perform compared to each other. This makes it possible to find the best set-up. The total numbers of real detected passes and the detections of the simulations are comparable with respect to the (outdated) space population model of PROOF from 2009.

5. Stare and Chase

Section 3.1 describes the method for initial detection of objects orbiting Earth. In order to distinguish stars from objects in images taken by the staring camera the images are analyzed in an image processing algorithm. The following sections describe the requirements of a functional system, the image processing algorithm and the recapturing through the telescope based on the gathered information of the staring cameras. In the end the accuracy of the short time prediction is discussed.

5.1. Necessary resolution of a staring camera image

Especially for recapturing an RSO the resolution of the staring camera system is critical. It determines the precision for the estimated extrapolation of the object's trajectory mainly. The determination of the necessary image resolution is explained in the following in more detail:

Measuring uncertainties occur caused by adding the errors of the measurements themselves and the image processing. These uncertainties have influences on the prediction accuracy of the RSO coordinates and make it difficult to recapture the target with the telescope. Some uncertainties can be compensated for example by improving the algorithms for object determination. However, others are given by the system components like the response of the mechanical camera shutter or the timing accuracy of the GPS-timer.

A big contribution to the spatial accuracy is the resolution of the image, which is given by the focal length of a lens and the pixel size of a camera. Hence, a Monte Carlo simulation is used for determining the minimum focal length for a successful recapturing with respect to the used camera. The algorithm is based on a data array which stands for a coordinate system in the image plane with axes represented by image pixels of the staring camera image. Each pixel covers an angle in arc seconds depending on the image resolution which is presented in table 8 for eight different system settings.

Table 8: Resolution for different system settings.

Camera	f' = 200 mm	f' = 135 mm	f' = 85 mm	f' = 50 mm
Andor Zyla	6.7 "/px	9.93 "/px	15.77 "/px	26.81 "/px
FLI PL16803	9.28 "/px	13.75 "/px	21.84 "/px	37.13 "/px

Figure 36 shows an overlay of two sequential images of the staring camera to visualize the structure of the simulation algorithm. It is based on the used extrapolation method of the trajectories of real measurements (see subsection 5.3.1) which takes the starting and end points of the detected tracks. Therefore, these tracks are presented in the simulation just by their starting (p_{1s} and p_{2s}) and end points (p_{1e} and p_{2e}) in the data array of the image. Depending on the used exposure time t_e and the velocity of the passing RSO the track appears at different

lengths l_t. The gap time between the images and the velocity give the length of the gap l_{gap} between the two tracks. These correlations of the times and lengths are given in equation (5.1-1):

$$\frac{l_{gap}}{l_t} = \frac{t_{gap}}{t_e}. \tag{5.1-1}$$

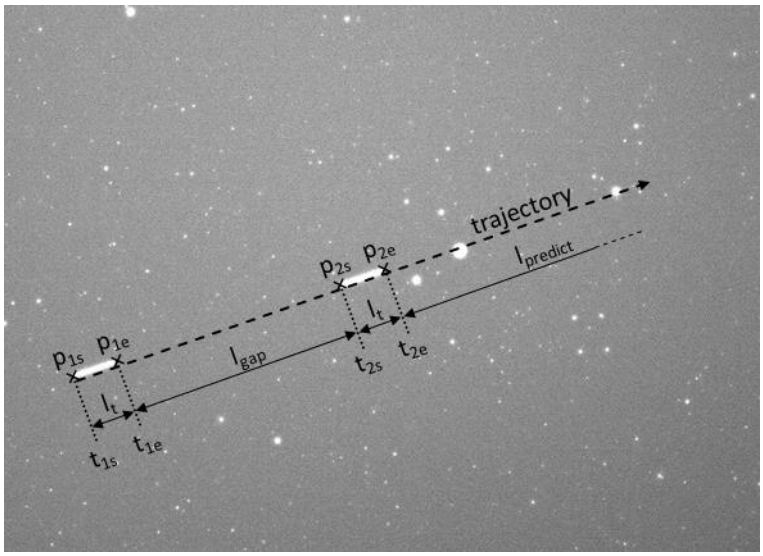

Figure 36: Overlay of two images showing a passing RSO with information about the gap length and track length.

A standard deviation of one pixel due to measurement errors is added to each of the four location points (starting and end points of the two tracks) in the image plane (black points in figure 37). Just as the position errors, time errors are causing additionally an inaccuracy of the data points. These depend for example on the camera to telescope synchronization. A deviation of the track length and the gap distance is caused by the timing error of the staring camera while the timing error of the synchronization leads to a changed distance between the tracks and the recapture position. Fitting a straight line to the four data points give the estimated trajectory of the orbiting object (blue lines in figure 37). The fitting algorithm and predicting the coordinates are the same as for the real recapture and are explained later in more detail in section 5.3. A loop with 10000 iterations of the fitting and predicting gives a point cloud of predicted locations shown in figure 37.

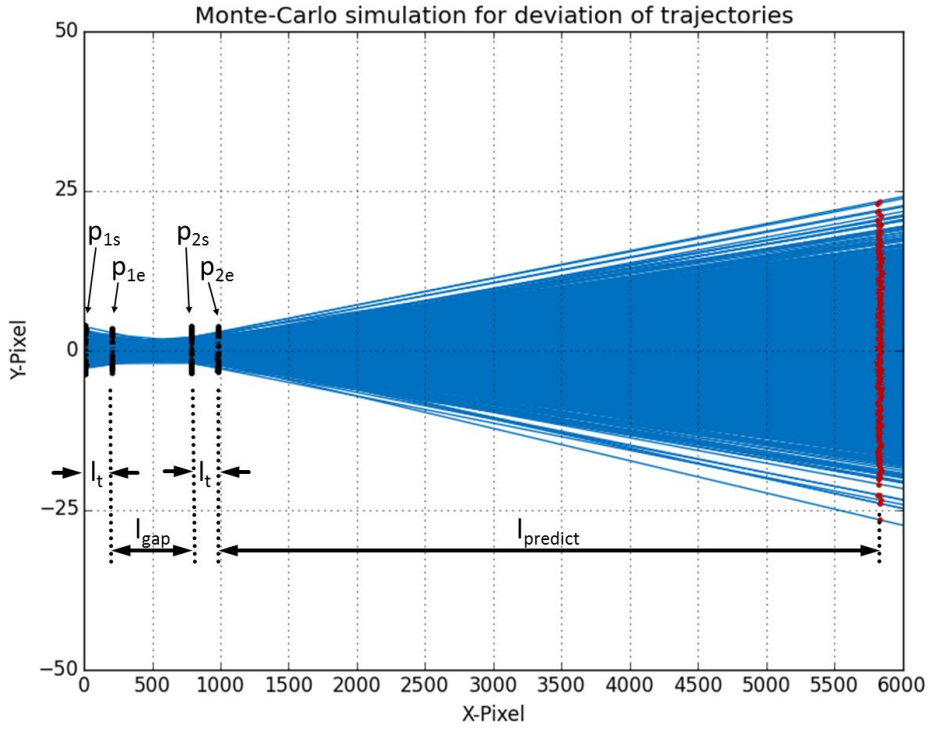

Figure 37: Monte- Carlo simulation of possible short-time object trajectory (blue) based on starting- and end-points of two tracks (black).

Figure 38 shows the resulting point cloud which can be divided into a standard deviation in x-direction (along track) and y-direction (cross track). Uncertainties have an effect on both directions where the uncertainty in time has greater contribution to the along track deviation.

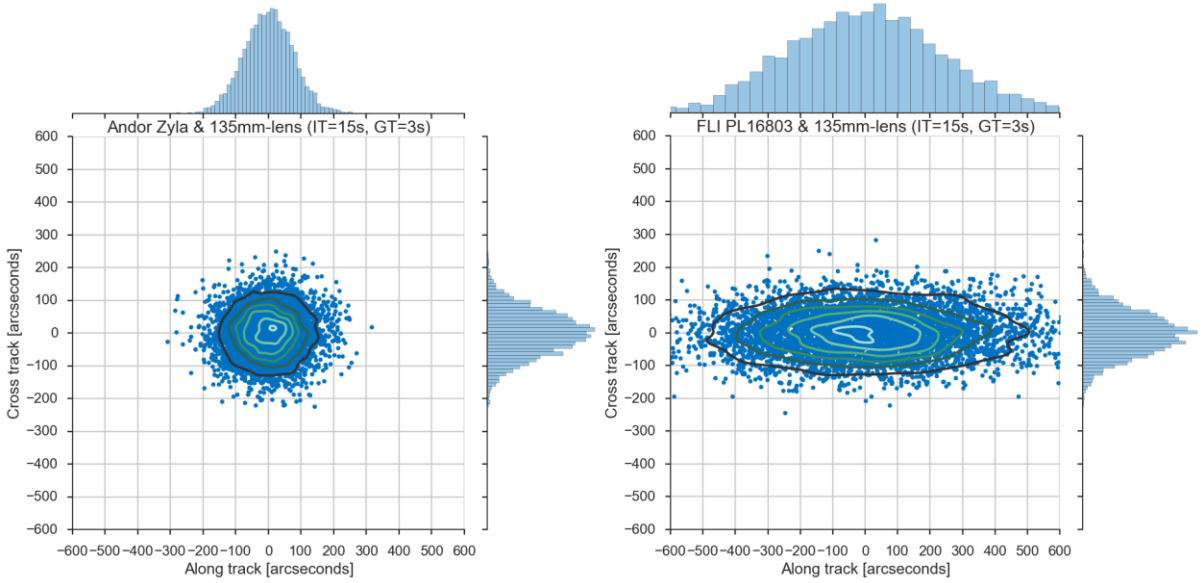

Figure 38: Point cloud of the prediction-deviation for the Andor Zyla (left) and the FLI PL16803 (right) camera with a 135mm camera lens. The interception head time (HT) is 15s and the gap time (GT) 3s.

Both plots are based on simulations for a headtime (HT) of 15 s and a gap time (GT) of 3 s between the two tracks. In order to give the deviations in arc seconds the scales of the axes are

adjusted. On the left side the Andor Zyla and on the right side the FLI PL16803 camera both with a 135 mm camera lens are shown. Noticeable is the much higher along track deviation of the FLI camera caused by the long shutter times (almost 40ms) due to the mechanical shutter. In order to determine if the prediction accuracy is sufficient enough for recapture an RSO with a telescope the standard deviations of the point clouds for along and cross track can be used. In order to capture 99.7% of the detected objects by the staring camera the standard deviation in arc seconds has to be multiplied by three. Table 9 presents the quantities of the along and cross track (AT resp. CT) for different systems, interception times and gap times.

Table 9: Results of the Monte-Carlo simulation for different systems (in arc seconds) for along (AT) and cross track (CT). Green means a recapturing probability of 99 % with a Telescope in the center of the FOV (0.1°). Yellow, object will be in FOV (0.3°). Red, a recapturing is not possible.

		Andor Zyla									FLI PL 16803							
200mm Lens	Interception time	GT = 2		GT = 3		GT = 4		GT = 5		Interception time	GT = 2		GT = 3		GT = 4		GT = 5	
		AT	CT	AT	CT	AT	CT	AT	CT		AT	CT	AT	CT	AT	CT	AT	CT
	10	156	140	111	95	87	71	72	59	10	1197	195	691	131	488	99	376	80
	15	228	202	157	133	123	102	101	81	15	1764	286	992	186	697	141	529	112
	20	300	268	205	175	159	129	128	104	20	2366	370	1314	243	907	181	700	143
	25	373	332	252	215	193	159	157	129	25	2942	453	1662	298	1136	223	860	178
	30	433	395	300	256	227	188	185	150	30	3525	545	1995	354	1360	258	1020	208
	35	514	454	347	298	265	219	215	174	35	4087	635	2295	409	1566	307	1176	240
135mm Lens	Interception time	GT = 2		GT = 3		GT = 4		GT = 5		Interception time	GT = 2		GT = 3		GT = 4		GT = 5	
		AT	CT	AT	CT	AT	CT	AT	CT		AT	CT	AT	CT	AT	CT	AT	CT
	10	235	211	162	138	128	107	108	87	10	1217	290	704	193	502	148	390	120
	15	336	303	232	202	180	150	149	121	15	1810	418	1023	274	715	208	545	167
	20	435	397	300	257	234	194	193	156	20	2419	546	1358	359	949	265	714	216
	25	549	494	372	324	285	238	232	190	25	2984	677	1694	446	1162	326	887	260
	30	652	582	444	386	336	280	273	221	30	3624	808	2035	522	1389	385	1051	308
	35	771	680	512	438	390	325	313	254	35	4213	939	2366	607	1639	453	1217	354
85mm Lens	Interception time	GT = 2		GT = 3		GT = 4		GT = 5		Interception time	GT = 2		GT = 3		GT = 4		GT = 5	
		AT	CT	AT	CT	AT	CT	AT	CT		AT	CT	AT	CT	AT	CT	AT	CT
	10	370	333	260	219	203	169	174	138	10	1274	461	754	308	543	235	430	191
	15	537	483	368	317	286	237	236	192	15	1893	665	1107	435	781	328	608	268
	20	706	633	486	408	373	309	304	248	20	2511	866	1454	575	1012	423	790	342
	25	863	778	593	510	456	374	366	300	25	3120	1073	1818	698	1261	522	968	414
	30	1050	938	706	596	539	451	433	359	30	3750	1299	2146	840	1504	618	1140	493
	35	1203	1072	812	705	619	517	498	408	35	4396	1479	2504	956	1740	700	1320	567
50mm Lens	Interception time	GT = 2		GT = 3		GT = 4		GT = 5		Interception time	GT = 2		GT = 3		GT = 4		GT = 5	
		AT	CT	AT	CT	AT	CT	AT	CT		AT	CT	AT	CT	AT	CT	AT	CT
	10	635	561	442	381	350	288	290	239	10	1461	767	903	522	670	399	545	325
	15	908	812	630	540	487	405	408	323	15	2191	1132	1327	749	956	554	756	447
	20	1201	1073	820	703	627	530	520	419	20	2875	1498	1717	966	1240	715	996	582
	25	1480	1318	1015	868	770	639	622	509	25	3484	1838	2117	1177	1536	890	1210	701
	30	1776	1579	1202	1021	899	754	741	596	30	4229	2172	2579	1424	1794	1047	1445	834
	35	2064	1825	1372	1178	1052	879	858	698	35	4959	2543	2976	1646	2088	1216	1650	965

The colors show a possible recapturing through a telescope within a FOV of 985.35 arc seconds like the one used by the DLR. Red fields indicate insufficient prediction accuracies while the yellow fields visualize a possible recapture of the RSO in the FOV. The green fields are showing a recapturing in the mid third of the telescope image (328.45”).

In conclusion, the FLI camera needs lenses with long focal length to compensate the high timing uncertainties caused by the mechanical shutter. Furthermore, none of the cameras can be

equipped with a 50 mm lens and a gap time between the image frames should not be shorter than 3 s except for the Andor Zyla / 200 mm combination. The longer the telescope needs to reach the point of interception the longer the headtime must be. This time should not be longer than 30 s for the Zyla and 10 s for the FLI camera.

5.2. PinPoint - Astrometric Engine

Important for the recapture of RSOs is an astrometry software which is responsible for a fast and precise determination of the pointing direction and transformation of the image coordinates into equatorial coordinates. The used software is explained in the following:

PinPoint is an astrometric engine which can be implemented in several computer languages for automated astrometry. Its major purpose is high speed astrometric image processing which is called plate solving by the program. However, the engine can be used for asteroid and comet searching or for supernova hunting as well [42].

Plate solving means that PinPoint analyses an image and tries to correlate the found stars in an image with the stars of a star catalog. It assigns each image pixel to an equatorial and horizontal coordinate, if there is a match. For short processing times approximated coordinates of the image center point and an image scale are necessary in advance.

As reference various star catalogs can be implemented. The difference of the catalogs is in the number of stars included with respect to the magnitude. For wider FOVs (wider than 15 arcminutes) the Guide Star Catalog [43] developed by the Association of Universities for Research in Astronomy has enough stars included. More dense catalogs are the United States Naval Observatory (USNO) catalogs [44] and allow having smaller FOVs which is needed for solving telescope images.

For the following image processing algorithms the stare and chase system uses PinPoint as plate solving engine. The initial center point coordinates of the images are manually given by the staring camera mount and the image scale by known lens and camera parameters.

5.3. Algorithm

The image processing algorithm is the core of a stare and chase system. Two algorithms are developed for different exposure times of the staring camera. These are using different methods for object determination and object assignment but the same for calculating the prediction. One algorithm can handle exposure times longer than 0.5 s (in the following: long) where the passing object appears as a track in an image. For exposure times shorter than 0.5 s (in the following: short) the RSOs are appearing as points between the stars and can be handled by the second algorithm. These two approaches are explained in detail the following subsections.

5.3.1. Long exposure times

The data processing of the staring camera images can be separated into three steps. It starts with the image processing algorithm to distinguish between stars and RSOs. A method to assign the detected objects in subsequent images is following. Finally, the calculation of the short time prediction has to be accomplished. These steps will be explained in the following in more detail. An overall block diagram for the algorithm is shown in figure 39.

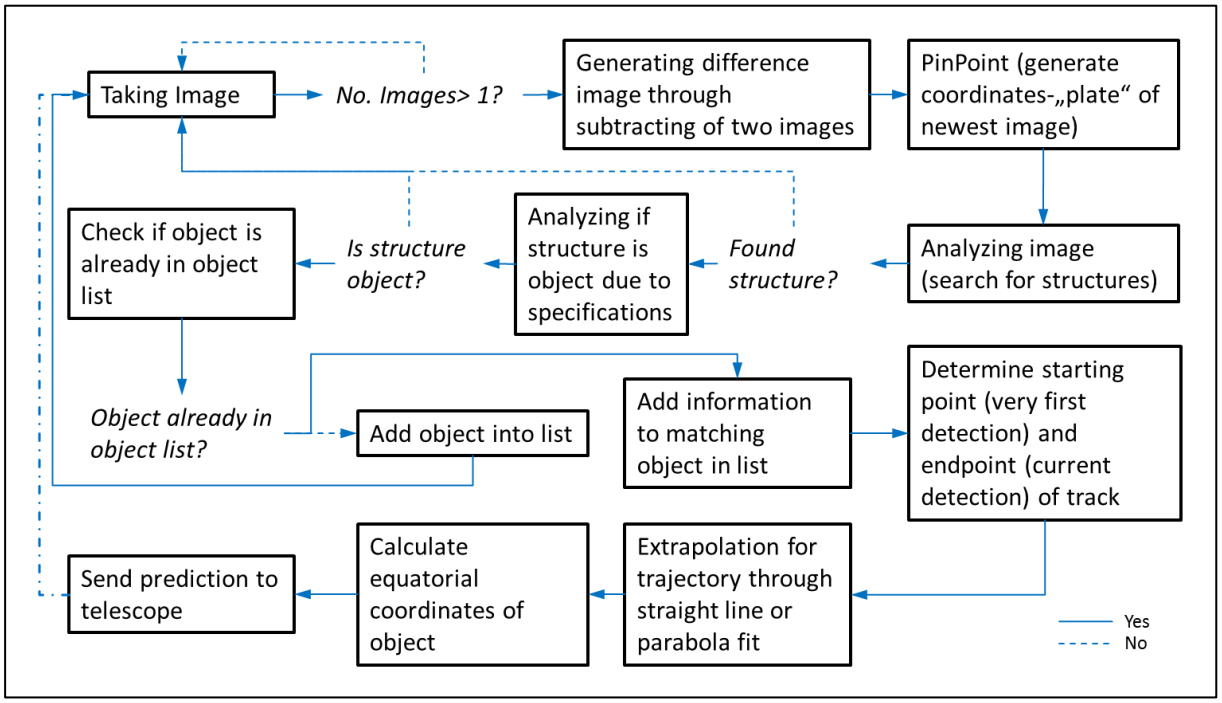

Figure 39: Block diagram for the image processing algorithm for long exposure times.

After starting the long exposure mode the staring camera is taking images continuously. In order to eliminate vignetting problems caused by the camera lens a difference image is generated through subtracting the last taken image from the second last one. Encountering this vignetting problem with this method leads to a decreasing signal-to-noise ratio because of the adding of noise from the two images. However, it is a very fast method which is needed to keep the processing time as short as possible. Additionally, a PinPoint plate of the last image is generated for a later assignment from pixel coordinates to equatorial coordinates. Following this, the image is binarized with an adjustable threshold above the background noise. This threshold is generated based on equation (5.3-1), where m is the mean of the grey-scale value, σ the standard deviation and f an adjustable factor (for the measurements later a factor of two was used).

$$threshold = m + \sigma * f \tag{5.3-1}$$

Now all remaining structures can be analyzed in respect of their shape, orientation and location. A structure is declared as an RSO if the aspect ratio is greater than a specific factor (depending

on the exposure time and the used lens). No detections of RSOs in the images lead to a restart of the algorithm.

It has to be determined if the RSO is "new" in the FOV of the staring camera or if it is already known after its verification. The orientation and location of the track give information, if the same object was detected in an earlier image. For new RSOs a new object file is generated while an object corresponding to an already existing file is just added to it. Two or more successive detections of the same object lead to the direction of the trajectory and a prediction about a future location can be done.

For the estimation of a future location of the RSO the starting points and end points of the detected tracks are determined and a straight line is fitted to them. The interception where the telescope recaptures the RSO is calculated through the time gap and distance between the very first and last location and the chosen headtime. Typical headtimes are between 10 s and 15 s. Based on the coordinate plate generated during the image processing the predicted location in pixel coordinates can be translated into the right ascension-declination system. This information together with the time of interception is sent to the telescope control. After sending the prediction the algorithm starts from the beginning while the telescope chases the new detected object. All new found RSOs during the recapture are saved in the objects list until the telescope is ready for the next recapture run.

5.3.2. Short exposure times

Some similar functions are used for the algorithm for short exposure times. However, the processing is set up in a completely different way because the RSOs are appearing like the stars as points in the image and the shape based determination cannot be used any more.

Different approaches for determining an RSO in a short exposure image are possible. One method is to generate a mask which fades out all the stars contained in a star catalog above a specific magnitude. Just RSOs would appear in resulting images. However, a problem is the wide FOV of the staring cameras and therefore the high number of stars contained in the image. Additionally, a continuous update of the mask due to the Earth's rotation and an update of the used magnitude level of the stars are necessary. This increases the processing time of the algorithm which has to be short for as short as possible headtimes. Another approach would be to stack a sequence of taken images and connect the found structures. A vector would be generated for each connection where the vectors connecting the stars have the same direction. For moving objects the vectors have different directions and can be extracted. Here, the disadvantage is the high number of images which have to be taken to eliminate false detections and therefore the longer processing times. Figure 40 shows the block diagram of the developed method which is explained in the following:

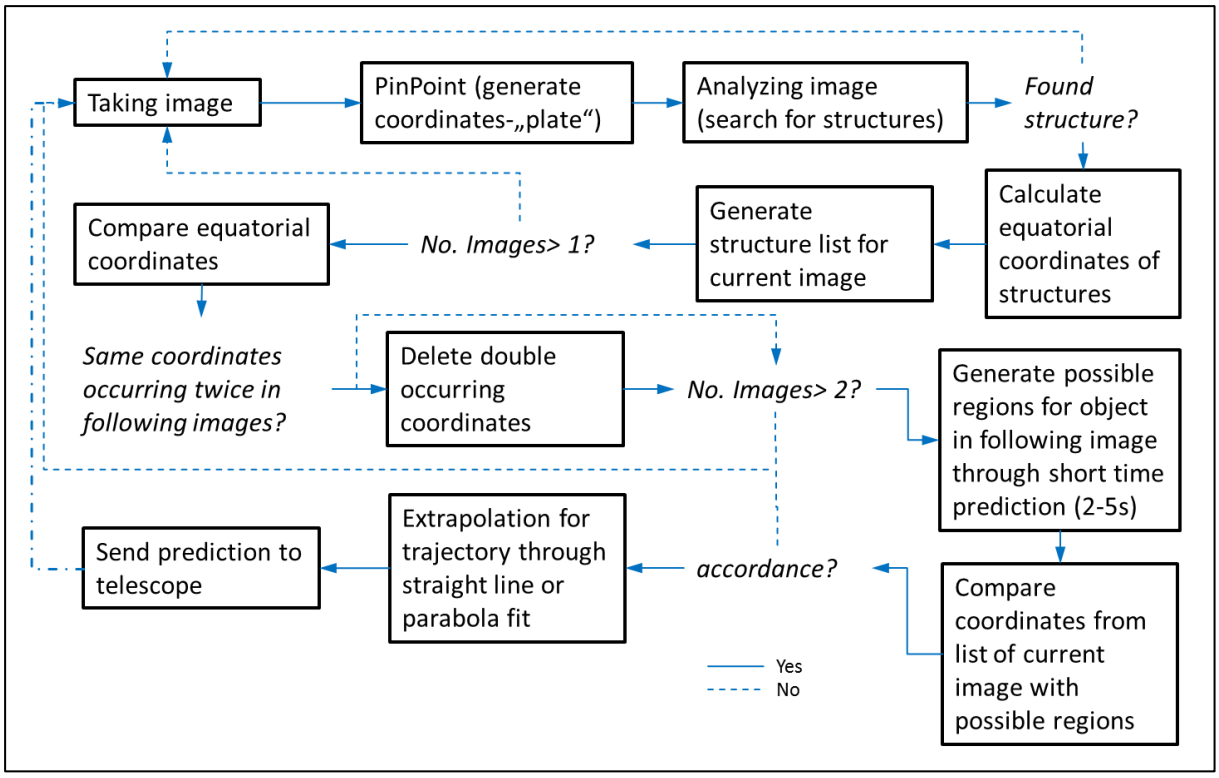

Figure 40: Block diagram for the image processing algorithm for short exposure times.

As for the algorithm for long exposure times the staring camera continuously takes images of the sky. PinPoint generates a plate for a later conversion of the image pixels to equatorial coordinates. In contrast the other processing algorithm, three images are necessary to determine an object reliably instead of two. Each image is analyzed for structures the same way as for long exposure times. The centers of gravity (COG) of the point like RSOs are used as location coordinates which can be determined more accurately than starting and end points of a track. This time each structure is assigned to its right ascension- and declination coordinate provided by the PinPoint plate and compared to the coordinates occurring in the image before. An RSO has different coordinates in each image due to its movement while the coordinates do not change and will be deleted if the structure is a star. In the end just moving objects remain. A third image is used to decrease the risk of false detections caused by stars occurring not in every image. This appears for example due to faint stars close to the threshold level of the binarization. The known coordinate information of each structure in the first two images allows generating a region where a possible object should be in third image. Three different equatorial coordinates of the structure in the three images and a location in one of the regions in the third image identifies the structure as an orbiting object. The assignment of the objects from various image series is also based on the equatorial coordinates. Each object determination contains due to the usage of three images the current location and two older locations of the RSO. An agreement of an old location from the current determination with locations of the detection from before verifies the same identity.

Finally the short time prediction can be calculated for recapture the detected RSO through the telescope. The estimation of the trajectory uses the same functions as for the algorithm which handles long time exposure times. For this algorithm, the extrapolation of the straight line is fitted onto three instead of four object locations, which however has no special effects to the prediction.

5.3.3. Advantages and Disadvantages for different exposure times

A determination of the beginning and end point of a track in an image causes inaccuracies which have to be encountered with additional algorithms. However, even with these algorithms the center of gravity leads to more precise spatial positions of the RSOs. A more accurate determination of the RSO's position as base of the extrapolation leads to a more accurate prediction for recapture. Therefore the algorithm for short exposure times gives better estimations of the trajectories of the RSOs. For long exposure times a determination of the location based on COG is not possible due to the length of the track. A shorter exposure time is resulting in a higher signal to noise ratio due to the adding thermal noise which increases the longer the exposure takes. Therefore, using short exposures can decrease the detectable object size. An advantage for the longer exposure time is the knowledge of a passing RSO immediately after one taken image. The possibility of false detections is decreased as well due to an easy determination of objects based on their aspect ratio.

In order to give an overview the advantages and disadvantages of both image processing methods are listed in table 10.

Table 10: Advantages and disadvantages for short and long exposure times

	Long exposure times	Short exposure times
Advantages	Object after one image detectable	Higher signal to noise ratio
	Decreased susceptibility for false detections	Object determination more precisely
Disadvantages	Lower signal to noise ratio	Object determination after three images possible
	Determination of starting- and endpoint of track not precise	Higher susceptibility for false detections
		PinPoint problems in twilight

For future space surveillance a combination of long and short exposure times with respect to the daytime and the affiliated algorithms is possible to obtain the advantages of both. At the beginning of an observation during twilight, a long exposure times can be used to verify the detection of enough stars in the image for using PinPoint. Later in the night the algorithm can be changed to short exposure times because the ambient light is sufficiently dark and fainter RSOs can be detected.

5.3.4. Comparison with TLE data

It is useful to know which object has been detected from the staring camera, especially if space surveillance is used to add new objects to an existing but incomplete database. For example if two RSOs are detected at the same time it is more important to recapture and measure the unknown one with the telescope. For determining the system's performance, information like the object's size is necessary as well. As soon as the objects identity is verified an access of the available object's data is given by SATCAT.

The stare and chase algorithm was adjusted to provide this needed information about the RSO by an alignment to the database. A prior initialization is necessary for an instant object verification due to the high number of RSOs contained in the TLE catalog. This gives a fast readable reference list of all already detected orbiting objects. After the detection of an object a comparison of its equatorial coordinates is done with the equatorial coordinates of each object in the reference list for the time of detection.

Based on this information the comparison of the PROOF simulations and the measurements are accomplished in section 4.7.

5.4. Recapturing of orbiting objects

A first successful series of recaptured RSOs took place in January 2016. The system was set up with the FLI PL16803 camera and the 135 mm f/2.0 lens. An exposure time for the streak detection was set to 1 s while a gap time between the images was 13 s due to the slow readout time of the camera. As staring camera direction a pointing at azimuth of 70 ° and an altitude of 50 ° were used. Figure 41 shows the detection of a track of a satellite in two subsequent images taken by the staring camera (left) and the "recaptured" object by the main telescope (right). The image processing algorithm was able to assign the detected track of the first image to the corresponding track in the second image and to extrapolate the trajectory for a short time prediction. Later analysis determined the object as GLOBALSTAR M003 (NORAD ID: 25165) at a range of 1922 km based on TLE information. In future, the high resolution image of the telescope can be used for more precise orbit determination. Space debris was detected with this Stare and Chase system as well, like a rocket body named SL-16 R/B (NORAD ID: 23343) at a range of 759 km [13].

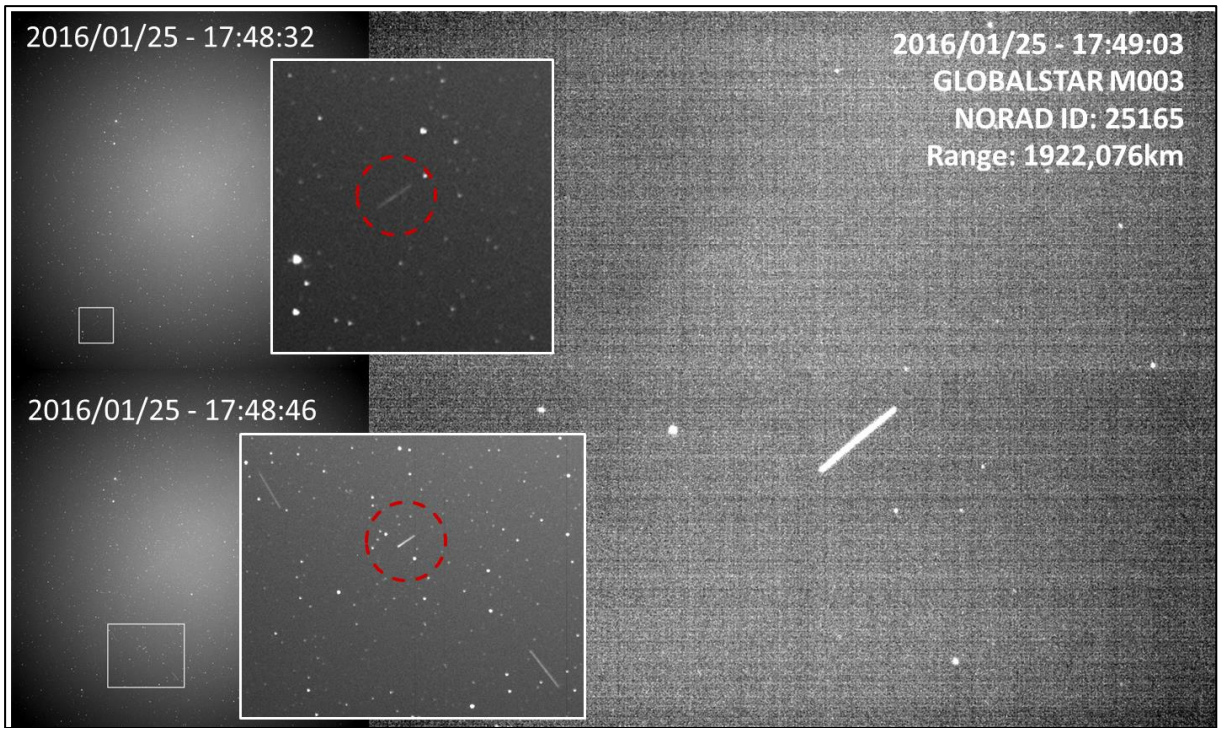

Figure 41: Successive images (exposure time 1s) of the staring camera (FLI PL16803 camera & 135mm f/2 lens) with tracks of the passing RSO (left). Image of the satellite GLOBALSTAR M0003 (NORAD ID: 25165) taken with the main telescope (right).

Furthermore, successful recapture measurements were performed using the image processing algorithm which can handle short exposure times (<0.5 s). For this "recapture"-test the system was set up with the Andor Zyla camera and the 135 m f/2.0mm lens. Gap times between the image frames were set to 3 s and the exposure time was 0.1 s. A prediction headtime of 10 s and a line of sight direction of 49 ° altitude and 333 ° azimuth were used. Figure 42 shows three images of the staring system (left) and the recaptured object through the telescope (right).

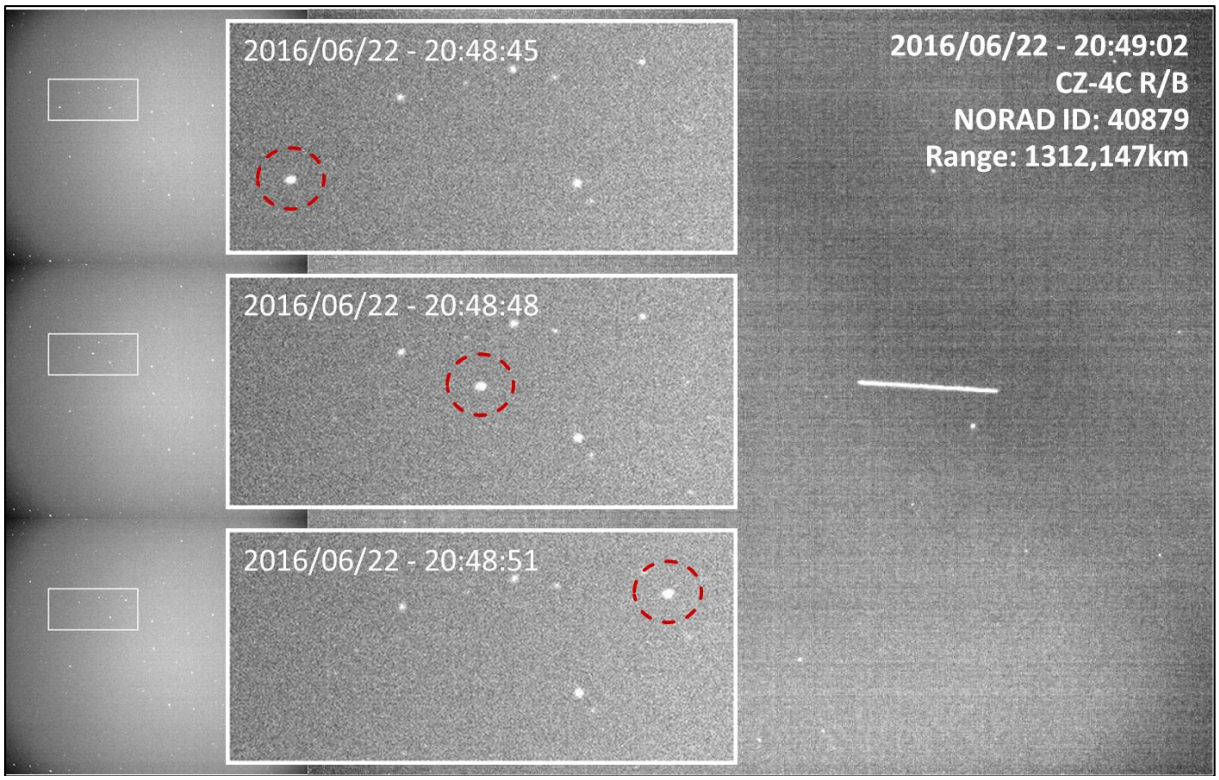

Figure 42: Successive images (exposure time 0.1s) of the staring camera (Andor Zyla camera & 135mm f/2 lens) with points of the passing RSO (left). Image of space debris CZ-4C R/B (NORAD ID: 40879) taken with the main telescope (right).

The captured RSO is space debris known as CZ-4C R/B (NORAD ID: 40879) at a range of about 1312 km from the DLR research observatory.

5.5. Accuracy of the predicted data

In order to analyze the prediction accuracy, the recaptures of the detected RSOs by the staring camera were measured with respect to the distance between the object's location in the image and the center of the image. In this case a staring system containing the Andor Zyla camera and the 135 mm f/2.0 lens was used. Between two images a gap time of 5 s occurs and the exposure time was set to 1 s. The maximum deviation of the objects to the image center for 20 measurements was 722 arcseconds which corresponds to three times the standard deviation like in the Monte Carlo Simulations in section 5.1. However, an along and cross track deviation is not given due to the random direction of the trajectories. Therefore the measured deviation is drawn as circle (red) in figure 43. As reference the FOV of the main telescope is visualized as a grey background.

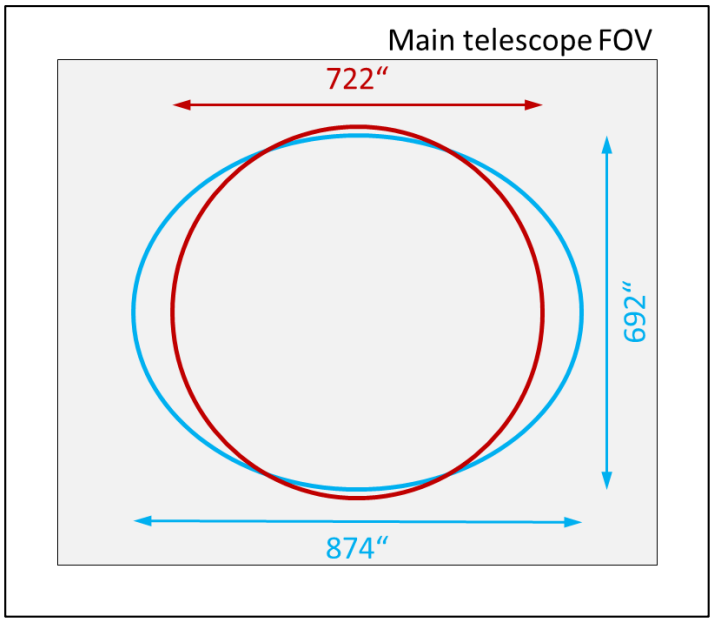

Figure 43: Predicted (blue) and real measurements (red) of the recapture accuracy. Dotted is the standard deviation of the measurements.

Using the Monte Carlo like simulation from section 5.1, with the system parameters as used here, the along track deviation is 874 arcseconds and the cross track deviation is 692 arcseconds (blue ellipse in figure 43). The values differ from the values given in table 9, which is due to a binning of the sensor pixels of the staring camera. This allows faster readout speeds at the expense of the resolution. Here, the binning is two but for the simulations in section 5.1 no binning was used. For the simulation a horizontal trajectory is set, which leads to the elliptical shape. The simulations are matching very well with the real measurements, which agrees with the results of the Monte Carlo simulations.

6. Outlook

For the presented stare and chase system improvements of the prediction algorithm are planned. Instead of using an extrapolation based on a straight line a preliminary orbit can be determined for example with the method presented in section 2.4. This orbit will also be valid just for a short time period due to the low resolution of the staring camera but a continuous tracking of the main telescope will be possible. It allows laser ranging to new detected RSOs which gives information about the distance to the object within the range of several meters. From the distance and the accurate measurements of the angular coordinates a precise orbit can be calculated. Another possibility to determine prior orbits with such a stare and chase system is using two staring cameras (or more) set up at different locations and pointing to the same region of sky. Parallax measurements allow determining the altitude of an object and therefore an additional quantity for the orbit estimation is given. With it other orbit determination algorithms described in reference [21] can be used. Furthermore, due to this additional parameter more accurate orbits are expected. However, this is subject of future analysis.

Further PROOF simulations will show the detection performance for different camera and lens combinations with the main goal of detecting smaller orbiting objects. Different observation sites can be simulated as well to determine where and how many facilities are necessary for a surveillance which is independent of weather and twilight conditions.

Designing camera lenses which are optimized for space surveillance applications could decrease the detectable object size even more. The major requirements would be to reach a small as possible f-number with focal lengths correlating to large FOVs. Another important demand is a low vignetting allowing detections of RSOs on the outer parts of the images. This lens design could be optimized to large chip sizes which are usual for astronomical cameras.

Another possibility to reduce vignetting without designing new lenses and subtracting images like in the used image processing algorithm would be flat fielding. Flat fielding describes the calibration of the used optical sensor per dividing the taken image by a calibration image. This calibration image is taken before the measurements starts and can be a stack of very bright images with a high signal-to-noise ratio from the inside of the dome. It is also possible to generate such a calibration image of stacked exposures of the dawn or the dusk. [36]

Furthermore, the staring system can be improved in respect to the covered observation area through upgrading it to a multi staring system with more than one camera. One example of such a system is shown in detail in the following:

6.1. Multiple staring system for orbital surveillance (multi eye system)

To cover an even wider region of the sky a system consisting of multiple staring cameras can be thought of. Such a “multi eye system” combines the advantage of a large FOV with good detection efficiency for small orbiting objects.

The number of used cameras can be varied and depends just on the computing power of the image processing computer and the telescope slew rate. However, both problems can be bypassed for example by using several computers which process the images of the staring cameras. Each sends the predicted coordinates of a detected object to the telescope which executes one position after another. More than one RSO could be detected at the same time due to the large number of LEO objects and the wide FOV. In order to prevent this issue a priority list has to be generated for the detected RSOs. Each object is stored in a database. Immediately after a detection in a staring camera image, the found object is analyzed and gets a high priority if it is a new object or a low priority if it is already known. Objects with the highest priority are recaptured first. Additionally other prioritizations are imaginable.

6.1.1. Orientation of the cameras

Most important is the orientation of the staring cameras which can easily be expanded by using multiple staring cameras. In order to avoid long telescope moving distances after a detection of an RSO and therefore long times until interception (in the following: headtime) a circular arrangement of the individual staring FOVs is supposed with an initially telescope direction to the center point. The alignments of the cameras cause due to the rectangular or square shaped FOVs a polygonal shaped observation region. An example for a multi staring system with five cameras is given in figure 44.

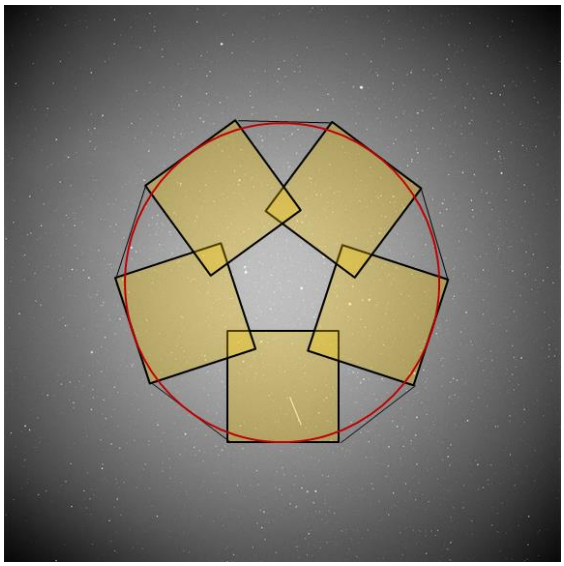

Figure 44: Orientation of five cameras of a multi "staring" system (yellow) and the covered region, as well as an approximation of the covered region to a circle (red).

As for single camera systems, the closer the elevation of the LOS to horizon the more objects are passing the FOV. However, the detection efficiency decreases (see section 4.3) which makes the zenith to the best solution as center of the covered region. Table 11 shows the huge surveillance area for different set-ups of a multi eye system in square degrees, steradian and the diameter in degree for an approximation to a circle (red in figure 39). Gaps like the center belong to the covered region because the object will be detected after or before the passing due to the trajectories of the RSOs. Therefore these areas are included in the area of surveillance

Table 11: Covered region of a multi-eye system in diameter and area.

No. of cameras	FOV = 5.5°			FOV = 10°			FOV = 15.5°		
	Dia. [deg.]	Area [deg.^{2}]	Area [sr.]	Dia. [deg.]	Area [deg.^{2}]	Area [sr.]	Dia. [deg.]	Area [deg.^{2}]	Area [sr.]
5	16.05	202.22	0.0615	29.17	668.47	0.2025	45.22	1606.16	0.4830
7	18.61	272.13	0.0827	33.84	899.58	0.2720	52.46	2161.24	0.6469
9	21.07	348.81	0.1060	38.32	1153.09	0.3480	59.39	2770.29	0.8250

Performances regarding the detectable object size remain unchanged to a single camera system but the larger observation area in sky allows detecting more RSOs. Table 12 shows the theoretical number of various, FOV-passing TLE objects per day and in one year based on the TLE-catalog (about 15500 entries in 2016) for different staring systems. Compared are systems set-ups with single cameras to multi staring systems containing 5 cameras. The systems are pointing to zenith and the effective FOVs are approximated by circles.

Table 12: Number of passing TLE objects for different staring systems. The total number of objects in the TLE catalog is about 15500.

No. cameras	FOV = 5.5° × 5.5°		FOV = 10° × 10°		FOV = 15.5° × 15.5°	
	1 day	1 year	1 day	1 year	1 day	1 year
1	1123 (1)	12720 (32.9)	2233 (1)	13248 (61.5)	3422 (1)	13334 (93.7)
5	3153 (1)	13285 (86.6)	5480 (1)	13390 (149.4)	7977 (1)	13465 (216.3)

Per day, the number of passing objects (all altitudes) is more than doubled if 5 cameras are used instead of one. In one year the numbers are similar but a multi staring system would be able to detect each object more often. The values in brackets are giving the average number of detections per RSO. Of course not all of these passing objects will be detected during the day because of the daylight and optical conditions.

6.1.2. Costs of a multi-eye system

Another crucial issue is the cost of such a multi eye system. One advantage compared to radar surveillance is the low costs of the optical counterpart. The different costs of the lenses in the range of 900 € to 10200 € (as of 2016) should be considered before setting up such s system. Table 13 will help to see the differences in the price for the different set-ups.

Table 13: Prices of multi-eye systems (as of 2016).

No. of cameras	Camera	FOV = 5.5 ° × 5.5 °		FOV = 10 ° × 10 °		FOV = 15.5 ° × 15.5 °	
		Focal length	Costs	Focal length	Costs	Focal length	Costs
5	Andor Zyla	135 mm	49,500 €	85 mm	53,500 €	50 mm	51,500 €
	FLI PL16803	400 mm	86,000 €	200 mm	64,500 €	135 mm	39,500 €
7	Andor Zyla	135 mm	69,300 €	85 mm	74,900 €	50 mm	72,100 €
	FLI PL16803	400 mm	120,400 €	200 mm	90,300 €	135 mm	55,300 €
9	Andor Zyla	135 mm	89,100 €	85 mm	96,300 €	50 mm	92,700 €
	FLI PL16803	400 mm	154,800 €	200 mm	116,100 €	135 mm	71,100 €

As in table 7 staring cameras with FOVs of about 5.5 ° are included as well. It would be possible to expand the FOV of one FLI camera from about 10 ° to 15.5 ° with saving 40 % of the costs due to the very cheap 135 mm and expensive 200 mm lenses. The performance would decrease just slightly as shown in figure 34 of the section 4.6.

7. Conclusion

The growing number of objects orbiting Earth increases the risk of collisions. In order to avoid close approaches of debris with active satellites or manned spacecraft a database with orbit information about the pieces is desirable. However, the orbits change constantly for example due to space weather conditions which makes is necessary to set up a large network of space surveillance facilities. Besides radar stations passive and active optical systems are very effective and allow building up such a network due to the low costs compared to radar stations. Disadvantages of optical space surveillance like the dependence of weather or light conditions can be encountered by setting up such a network spread around the world. An approach for a passive optical system for initial detection of RSOs was presented in this work.

In order to develop a staring system which is able to detect as small as possible RSOs, simulations with the simulation tool PROOF by ESA were done. PROOF based analysis of the observation times and staring camera pointing directions resulted in fundamental parameter specifications for further simulations. A passive optical observation campaign can be realized from dusk until dawn. However, the first 1.5 h after sunset and the last 1.5 h before sunrise (might change for other observation epochs) is a detection of an object in April impossible according to PROOF simulations. This is caused by the ambient light at the observation site during this time. The possible observation times during one year were analyzed as well. Observations are possible during the entire night in the months between April and September, while a temporal gap occurs during the other months because of the objects trajectories in the Earth's shadow. Further simulations showed how the detection efficiency changes for different pointing directions. While the number of passing objects rises for pointing directions getting closer to horizon the number of detections keeps the same due to the propagation of the light through a thicker atmospheric layer.

Based on the observation time and pointing direction different set-ups were analyzed with the simulation tool in addition to general considerations to the optical performance. Calculations showed the dependence of the detectable object sizes regarding the parameters of the lenses equipped to the staring camera. The aperture has the strongest influence while the focal length also affects the detectable size. An optimal lens for space surveillance would have a huge aperture for collecting as much light as possible. However, a short focal length for a slow movement of the object's image over the camera sensor is beneficial as well. These calculations are in agreement with simulated lenses. Finally, PROOF simulations with off-the-shelf lenses were performed. In order to determine the lens parameters which are necessary for the simulations the lens designs, based on a patent research, were analyzed with the optical ray trace software ZEMAX. According to the results of the PROOF simulations it can be assumed that

the combination of the FLI PL16803 camera and a 135 mm f/2.0 lens is a good system for LEO surveillance. Its large FOV compensates the weakness for detecting small objects. If the focus is on detecting small objects the Andor Zyla camera should be equipped with the 200 mm f/2 or 400 mm f/2.8 lens.

Comparisons of the simulated data with real measurements were showing the differences. With respect to the outdated space population model from 2009 used by PROOF and the increased number of RSOs (approx. 15 % since 2009), a similarity for the numbers of detections can be seen. Based on the object size differences occur between simulations and the observations. In contrast to the simulations, real measurements do not drop in the detection efficiency for RSOs larger than 2 m^2 in RCS. This saturation might be more likely than a decreasing detection efficiency. However, the sizes of the measured objects are based on measurements from radar facilities and are given in radar cross section and the PROOF output is a geometrical size in object diameter. Therefore the exact value of the RSO size where the saturation beginns can not be veryfied.

A minimum focal length of the lenses for a succesful recapture with respect to the used camera was determined with a Monte Carlo simulation. For the used FLI camera which has timing problems due to the mechanical shutter, the 200 mm lens would be the best sollution. The Andor Zyla is performing well with focal lenghs longer 135 mm. Measurements with the FLI camera and a 200 mm lens were compared with the simulations and were showing very similar results.

For determining passing objects in an image with a star background the programmed algorithms are performing very well. Both cases, for long and short exposure times, are detecting RSOs and are able to assign them to the correlating to one from prior images. For short time predictions in the range of 5 s to 15 s, the coordinate estimation based on a fit of a straight line to the measured coordinates with the staring camera is sufficiently precise. Several recaptures of orbiting objects were performed containing active satellites and space debris at different altitudes.

The presented stare and chase system is able to find unknown orbiting objects and generating sufficiently precise predictions of the objects trajectory for further measurements with a high resolution telescope. Already existing observation sites can easily be upgraded with a staring camera. Low costs and flexibility in adjusting the system to different requirements are reached with easy exchangeable off-the-shelf components. In combination with satellite laser ranging this system can be an alternative optical method for initial LEO surveillance. Its independence of prior information about RSO orbits and the wide FOV allows this system to support a buildup or maintenance of a space object catalog.

V. List of Figures

VI. List of Tables

VII. List of Equations

VIII. List of Abbreviations

CCD	Charged Couple Device
CMOS	Complementary metal-oxide-semiconductor
COG	Center of Gravity
DLR	Deutsches Zentrum für Luft-und Raumfahrt (German Aerospace Center)
ESA	European Space Agency
FHR	Fraunhofer Institute for High Frequency Physics and Radar Techniques
FLI	Finger Lakes Instrumentation
FOV	Field of View
FWHM	Full Width Half Maximum
GEO	Geostationary Orbit
GPS	Global Positioning System
GRAVES	Grand Réseau Adapté à la Veille Spatiale
ISS	International Space Station
LEO	Low Earth Orbit
LOS	Line Of Sight
MASTER	Meteoroid and Space Debris Terrestrial Environment Reference
MEO	Medium Earth Orbit
NASA	National Aeronautics and Space Administration
NORAD	North American Aerospace Defense Command
PPS	Pulse-per-Second
PROOF	Program for Radar and Optical Forecasting
PSF	Point Spread Function
RCS	Radar Cross Section
RMS	Root Mean Square
RSO	Resident space objects
SATCAT	Satellite Catalog
SLR	Satellite Laser Ranging
SSN	Space Surveillance Network
SSS	Space Surveillance System
TIRA	Tracking and Imaging Radar
TLE	Two Line Element
TTL	Transistor-Transistor-Logic
UFO	Uhlandshöhe Forschungs Observatorium
USNO	United States Naval Observatory
UTC	Coordinated Universal Time

IX. Eidesstattliche Erklärung

Hiermit versichere ich, an Eides statt, dass ich die vorliegende Masterarbeit mit dem Titel Initial Detection and Tracking of Objects in Low Earth Orbit selbständig und ohne fremde Hilfe verfasst und keine anderen als die angegebenen Hilfsmittel benutzt habe. Die Stellen der Arbeit, die dem Wortlaut oder dem Sinne nach anderen Werken entnommen wurden, sind in jedem Fall unter Angabe der Quelle kenntlich gemacht. Die Arbeit ist noch nicht veröffentlicht oder in anderer Form als Prüfungsleistung vorgelegt worden.

04.10.2016

.....

Datum Unterschrift

X. Bibliography

[1] J.-C. Liou, „Update on Three Major Debris Clouds," *Orbital Debris Quarterly News,* Nr. 14(2), p. http://orbitaldebris.jsc.nasa.gov/, April 2010.

[2] J.-C. Liou, „Increase in ISS Debris Avoidance Maneuvers," *Orbital Debris Quarterly News,* Nr. 16(2), p. http://orbitaldebris.jsc.nasa.gov/, April 2012.

[3] P. Anz-Meador, „Top Ten Satellite Breakups Reevaluated," *Orbital Debris Quarterly News,* Nr. 20(1&2), p. http://orbitaldebris.jsc.nasa.gov/, April 2016.

[4] NASA, Headquarters Office of Safety and Mission Assurance, „Handbook for Limiting Orbital Debris," NASA, Washington, DC, approved 2008.

[5] Center for Space Standarts & Innovation (CSSI), „NORAD Two-Line Element Sets," [Online]. Available: https://celestrak.com/.

[6] J. Shell, „Optimizing orbital debris monitoring with optical telescopes," 2010 AMOS Conference, Maui, Hawaii, 2010.

[7] M. Laas-Bourez et al., "A new algorithm for optical observation of space debris with the TAROT telescopes," Advances in Space Research, Volume 44, 2009.

[8] W. Jian-li et al., „Large FOV Mobile E-O Telescope for Searching and Tracking Low-orbit Micro-satellites and Space Debris," CNKI Journal, Chinese Journal of Optics, 2011.

[9] L. Cibin et al., „Wide Eye Debris telescope allows to cataloque objects in any orbital zone," Mem. Soc. Astron. It. Suppl., Volume 20, 2012.

[10] M. Boër, „The MetaTelescope: a System for the Detection of Objects in Low and Higher Earth Orbits," 2015 AMOS Conference, Maui, Hawaii, 2015.

[11] J. Gelhaus, S. Flegel und C. Wiedemann, „Final Report - Program for Radar and Optical Observation Forecasting," Institute of Aerospace Systems (TU Braunschweig), Braunschweig, 2011.

[12] J. Virtanen et al., „Streak detection and analysis pipeline for space-debris optical images," Advances in Space Research, Volume 57, 2015.

[13] T. Schildknecht, „Optical surveys for space debris," Springer-Verlag, Bern, 2007.

[14] P. Anz-Meador, „Monthly Number of Objects in Earth Orbit by Object Type," *Orbital Quarterly News,* p. http://orbitaldebris.jsc.nasa.gov/, April 2016.

[15] Inter-Agency Space Debris Coordination Committee, „IADC Space Debris Mitigation Guidelines," Action Item number 22.4, 2007.

[16] H. Klinkrad, Space Debris - Models and Risk Analysis, Berlin: Springer- Verlag, 2006.

[17] R. S. Jakhu und J. N. Pelton, Small Satellites and Their Regulation, New York: Springer Science & Business Media, 2013.

[18] NASA, Office of Safety and Mission Assurance, „Guidelines and Assessment Procedures for Limiting Orbital Debris," Washington, D.C., 1995.

[19] R. B. Thompson und B. F. Thompson, Astronomy Hacks: Tips and Tools for Observing the Night Sky, 1 Hrsg., Sebastopol, CA: O'Reilly Media, Inc, 2005, p. 412.

[20] Wikipedia, [Online]. Available: https://de.wikipedia.org/wiki/Astronomische_Koordinatensysteme. [Zugriff am 24 August 2016].

[21] R. R. Bate, D. D. Mueller und J. E. White, Fundamentals of Astrodynamics, New York, New York: Dover Publications, Inc, 1971, p. 455.

[22] Deutsches SOFIA Institut, „Atmosphärische Fenster," [Online]. Available: https://www.dsi.uni-stuttgart.de/bildungsprogramm/lehrmaterial/ir-strahlung/ir-fenster.html. [Zugriff am 24 August 2016].

[23] University of Georgia, „Physics and Astronomy @ UGA," [Online]. Available: http://www.physast.uga.edu/~rls/1010/ch6/ovhd.html. [Zugriff am 23 05 2016].

[24] European Space Agency (ESA), „Optical Ground Station," [Online]. Available: http://sci.esa.int/sci-fmi/36520-optical-ground-station/. [Zugriff am 15 August 2016].

[25] U.S. Air Force, „Space Surveillance Sensors: The FPS-85 Radar," [Online]. Available: https://mostlymissiledefense.com/2012/04/12/the-fps-85-radar-april-12-2012/. [Zugriff am 15 August 2016].

[26] G. E. Musgrave, A. Larsen und T. Sgobba, Safety Design for Space Systems, Oxford: Butterworth- Heinemann, 2009, p. 992.

[27] J. N. Pelton, New Solutions for the Space Debris Problem, Washington: Springer, 2015, p. 94.

[28] G. D. Badhwar und P. D. Anz-Meador, „Relationship of Radar Cross Section to the Geometric Size of Orbital Debris," AIAA/NASA/DOD Orbital Debris Conference, Baltimore, Maryland, 1990.

[29] J. Degnan, „Satellite Laser Ranging: Current Status and Future Prospects," IEEE - Geoscience and Remote Sensing Society, Volume GE-23, 1985.

[30] D. Hampf et al., „First successful satellite laser ranging with a fibre-based transmitter," Advances in Space Research, Volume 58, 2016.

[31] U. Renner, J. Nauck und N. Balteas, Satellitentechnik: Eine Einführung, Berlin: Springer-Verlag, 2013.

[32] PlaneWave, „AstroPixels.com," [Online]. Available: http://astropixels.com/bifrost/cdk17.html. [Zugriff am 05 July 2016].

[33] Finger Lakes Instruments, „Finger Lakes Instruments website," [Online]. Available: http://www.flicamera.com/proline/index.html. [Zugriff am 18 June 2016].

[34] Andor, „Andor website," [Online]. Available: http://www.andor.com/scientific-cameras/neo-and-zyla-scmos-cameras/zyla-55-scmos. [Zugriff am 18 June 2016].

[35] D. Hampf et al., „Aufklärung in Orbit: Detektion und Bahnbestimmung mit optischen Teleskopen," Stuttgart, 2013.

[36] S. B. Howell, Handbook of CCD Astronomy, Bd. II, Cambridge: Cambridge University Press, 2006.

[37] S. Arata, „JP,2012-247451.A". Japan Patent 2012-247451, 13 12 2012.

[38] M. Satoshi, „JP,2011-253050,A". Japan Patent 2011-253050, 15 12 2011.

[39] S. Flegel, "Maintenance of the ESA MASTER Model," Final Report, 21705/08/D/HK, TU Braunschweig, Institute of Aerospace Systems, 2011.

[40] J. Gelhaus, S. Flegel und C. Wiedemann, „Program for Radar and Optical Observation Forecasting," European Space Agency, Braunschweig, 2011.

[41] P. Wagner, H. Daniel und R. Wolfgang, „Passive optical space surveillance system for initial LEO object detection," 66th International Astronomical Conference, Jerusalem, Israel, 2015.

[42] DC-3 Dreams, Advances Observatory Software, „PinPoint Engine V6.0 Reference Guide," DC-3 Dreams.

[43] The Association of Universities for Research in Astronomy, Inc., „The Guide Star Catalog v1.1," The Association of Universities for Research in Astronomy, Inc., January 2001. [Online]. Available: http://gsss.stsci.edu/zzzOldWebSite/gsc/gsc1/gsc11/README11.HTML. [Zugriff am 21 September 2016].

[44] United States Naval Observatory, „The United States Naval Observatory (USNO) - Naval Oceanography Portal," U.S. Navy, [Online]. Available: http://www.usno.navy.mil/USNO. [Zugriff am 21 September 2016].

XI. Appendix

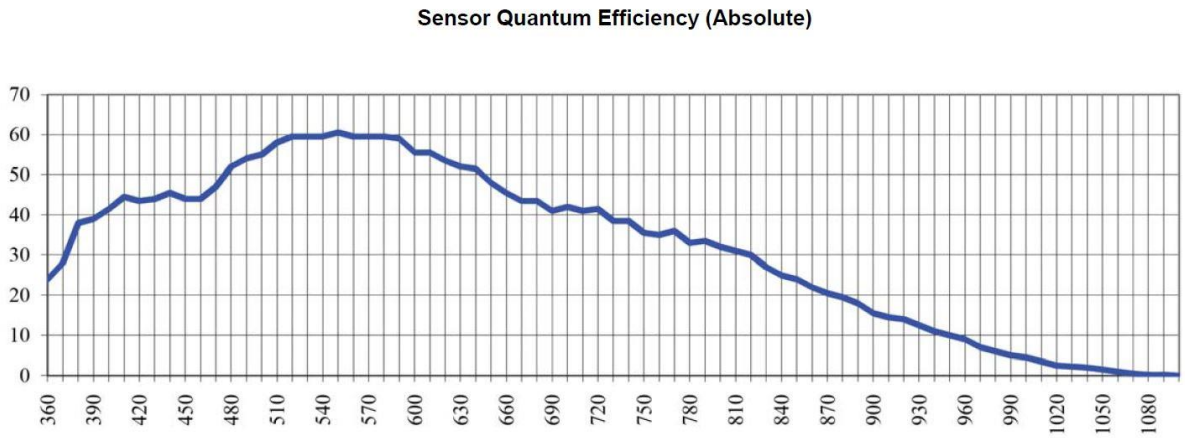

Appendix 1:Quantum efficiency of the FLI PL16308 camera.

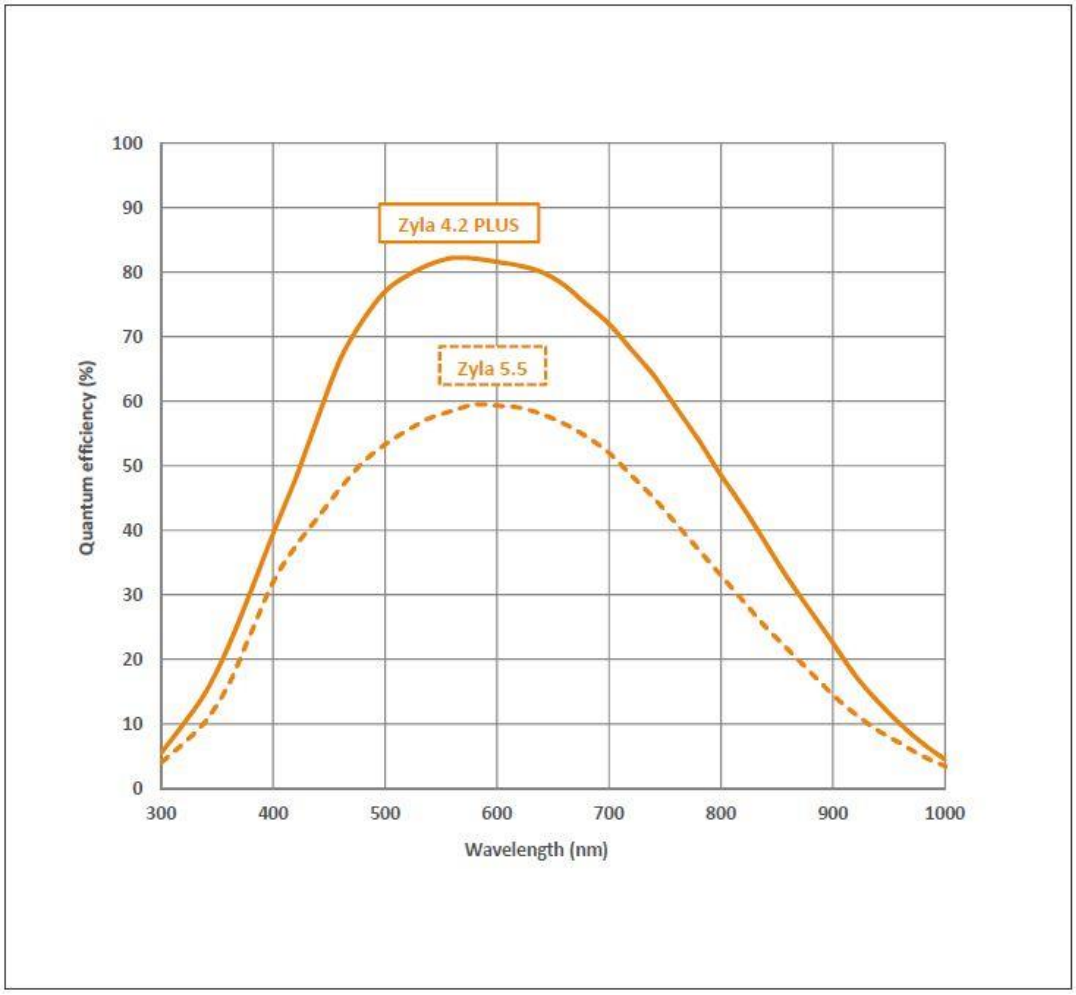

Appendix 2: Quantum efficiency of the Andor Zyla 5.5 camera (dotted line).